

# SSI-DM: Singularity Skipping Inversion of Diffusion Models

Chen Min <sup>\*1</sup> Enze Jiang <sup>\*1</sup> Jishen Peng <sup>\*1</sup> Zheng Ma <sup>1</sup>

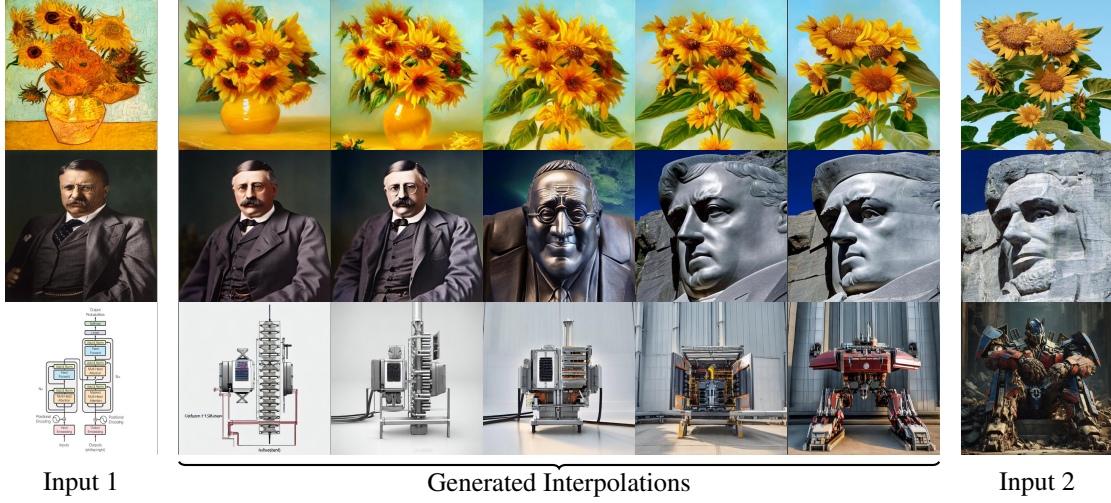


Figure 1. Interpolations of real images with diverse styles and kinds based on Stable Diffusion using SSI-DM.

## Abstract

Inverting real images into the noise space is essential for editing tasks using diffusion models, yet existing methods produce non-Gaussian noise with poor editability due to the inaccuracy in early noising steps. We identify the root cause: a mathematical singularity that renders inversion fundamentally ill-posed. We propose Singularity Skipping Inversion of Diffusion Models (SSI-DM), which bypasses this singular region by adding small noise before standard inversion. This simple approach produces inverted noise with natural Gaussian properties while maintaining reconstruction fidelity. As a plug-and-play technique compatible with general diffusion models, our method achieves superior performance on public image datasets for reconstruction and interpolation tasks, providing a principled and efficient solution to diffusion model inversion.

## 1. Introduction

Diffusion models have emerged as a dominant paradigm in generative modeling (Ho et al., 2020; Song et al., 2021a; Karras et al., 2022), enabling diverse image editing applications (Saharia et al., 2022; Kawar et al., 2023; Brooks et al., 2023; Tumanyan et al., 2023). Many of these applications often require inverting real images back into the noise space of pretrained diffusion models. Unlike VAEs (Kingma & Welling, 2013) or GANs (Goodfellow et al., 2014) with explicit latent representations, diffusion models lack an inherent latent space for real images, making accurate image-to-noise inversion *essential*.

The standard DDIM inversion (Song et al., 2021a; Dhariwal & Nichol, 2021) simply reverses the sampling process but suffers from a critical limitation: inverted noise deviates significantly from Gaussian distributions, exhibiting structural correlations that severely compromise editability (Staniszewski et al., 2024). Despite efforts to improve inversion through iterative refinement (Garibi et al., 2024), optimized embeddings (Mokady et al., 2023), or specialized numerical schemes (Huberman-Spiegelglas et al., 2024), the fundamental causes of inversion inaccuracy require further investigations.

In this work, we identify one of the *root causes* of this inaccuracy: a mathematical singularity in the score

<sup>\*</sup>Equal contribution <sup>1</sup>School of Mathematical Sciences, Shanghai Jiao Tong University, Shanghai, China. Correspondence to: Zheng Ma <zhengma@sjtu.edu.cn>.

function. When the data distribution is concentrated on low-dimensional manifolds—as is typical for natural images—the score function exhibits singular behavior near  $t = 0$  (Lu et al., 2023; Liu et al., 2025), rendering the inversion problem fundamentally ill-posed.

We propose *Singularity Skipping Inversion of Diffusion Models* (SSI-DM), a simple yet effective solution that bypasses the singular region. Instead of relying on sophisticated numerical techniques, SSI-DM simply adds a small amount of Gaussian noise to the input image, effectively skipping the singular region near  $t = 0$  where inversion is ill-posed, then proceeds with standard reverse-time integration. This skipping technique is trivial to implement—requiring only a single forward diffusion step—yet produces inverted noise with natural Gaussian properties while preserving reconstruction fidelity. Remarkably, SSI-DM is a plug-and-play technique compatible with pretrained diffusion models across diverse frameworks—DDIM (Song et al., 2021a), EDM (Karras et al., 2022), and Stable Diffusion (Rombach et al., 2022)—achieving superior performance without requiring iterative refinement or additional optimization.

**Our contributions.** (1) We provide mathematical and numerical justification showing that score function singularity at  $t = 0$  is a fundamental cause of inversion failures. (2) We introduce SSI-DM, a simple yet principled method that bypasses the singular region. (3) We present comprehensive experiments on pretrained models across LSUN Bedroom-256/Cat-256, ImageNet-256, and Stable Diffusion, demonstrating state-of-the-art reconstruction and interpolation quality with superior efficiency.

## 2. Related Work

**Image-to-noise inversion** Image-to-noise inversion is fundamental to key applications such as image editing (Kim et al., 2022; Hertz et al., 2023), interpolation (Dhariwal & Nichol, 2021), and inpainting (Zhang et al., 2023). For text-guided models, Null-text inversion (Mokady et al., 2023) optimizes null embeddings to minimize reconstruction error, while subsequent works improve upon this through enhanced embeddings (Dong et al., 2023; Miyake et al., 2025; Han et al., 2024) or by leveraging DDIM latents for guidance (Cho et al., 2024).

To reduce approximation errors, several methods have been proposed: ReNoise (Garibi et al., 2024) employs predictor-corrector schemes, EDICT (Wallace et al., 2023) uses coupled transformations, and others (Huberman-Spiegelglas et al., 2024; Brack et al., 2024) develop inversion techniques for non-probabilistic diffusion models. To enhance Gaussian properties, Parmar et al. (2023) introduce regularized outputs and Lin et al. (2024) optimize noise schedulers. Notably, Staniszewski et al. (2024) demonstrate that DDIM-

inverted latents exhibit non-Gaussian characteristics, with errors primarily concentrating in early noising steps.

**Singularity analysis in diffusion models.** The sampling process in diffusion models relies on approximating the score function  $\nabla_x \log p(x, \sigma)$ . When data is supported on a lower-dimensional manifold, the score function becomes singular as diffusion time approaches zero ( $t \rightarrow 0$ ). This phenomenon has been observed across multiple studies (Zhang & Chen, 2023; Chen et al., 2023c; Bortoli, 2022; Chen et al., 2023a; Stéphanovitch, 2025). Several works provide rigorous characterizations of this singularity structure. Pidstrigach (2022) establish lower bound estimates for the score function under low-dimensional manifold assumptions, while Chen et al. (2023b) derive singularity estimates for linear subspaces. Lu et al. (2023) employ Laplace’s method to provide a rigorous characterization of the singularity structure, which Liu et al. (2025) further extend to general frameworks.

## 3. Background

**Diffusion Models.** The sampling formulation of diffusion models has been thoroughly explained and generalized in prior works (Song et al., 2021b; Karras et al., 2022). For a general data distribution  $\mathbf{x}_0 \sim p_{\text{data}}$ , we consider a mollified distribution family  $p(\mathbf{x}; \sigma)$  obtained by adding independent Gaussian noise to  $\mathbf{x}_0$ :

$$\mathbf{x}_t = \mathbf{x}_0 + \sigma_t \mathbf{n}, \quad \mathbf{n} \sim \mathcal{N}(\mathbf{0}, \mathbf{I}), \quad (1)$$

where  $\sigma_t = \sigma(t) : [0, T] \rightarrow [0, \infty)$  is a strictly increasing noise schedule with  $\sigma_0 = 0$ . This distribution family gradually transforms the data distribution into Gaussian noise as  $t$  increases from 0 to  $T$ .

A scaling schedule  $s_t = s(t) : [0, T] \rightarrow [0, 1]$  is introduced for more generally sampling formats including DDIM, consider the scaled variable  $\tilde{\mathbf{x}}_t = s_t \mathbf{x}_t$ .

Two common choices are: (1) Variance Exploding (VE) SDEs with  $s_t = 1$ ; (2) Variance Preserving (VP) SDEs with  $s_t = 1/\sqrt{1 + \sigma_t^2}$ , where  $s_t$  is strictly decreasing with  $s_0 = 1$ . Without loss of generality, this article focuses on VE processes, with VP formulations provided in Appendix B. Since both variants share the same underlying mathematical structure, all theoretical analyses and methodological developments naturally extend to VP processes.

The general framework of sampling SDEs can be written as a sum of the probability flow ODE and a Langevin diffusion SDE:

$$\begin{aligned} d\mathbf{x} = & -\dot{\sigma}_t \sigma_t \nabla_{\mathbf{x}} \log p(\mathbf{x}; \sigma_t) dt \\ & \pm \beta_t \sigma_t^2 \nabla_{\mathbf{x}} \log p(\mathbf{x}; \sigma_t) dt + \sqrt{2\beta_t \sigma_t} d\omega_t, \end{aligned} \quad (2)$$

where  $\omega_t$  is a standard Wiener process and  $\beta_t = \beta(t)$  controls the relative rate at which existing noise is replaced with

new noise. The ‘+’ and ‘-’ signs correspond to separate SDEs for moving forward and backward in time, related through time-reversal (Anderson, 1982). The Fokker-Planck equation ensures that this SDE evolves within the smoothed distribution family  $p(\mathbf{x}; \sigma_t)$ , enabling the sampling task. Setting  $\beta_t = 0$  yields the probability flow ODE:

$$d\mathbf{x} = -\dot{\sigma}_t \sigma_t \nabla_{\mathbf{x}} \log p(\mathbf{x}; \sigma_t) dt, \quad (3)$$

where the score function  $\nabla_{\mathbf{x}} \log p(\mathbf{x}; \sigma_t)$  guides the denoising process. In practice, the score function is approximated using a neural network  $D_{\theta}(\cdot, \sigma_t)$  trained via denoising score matching. To sample from the data distribution, one initializes  $\mathbf{x}_T \sim \mathcal{N}(\mathbf{0}, \sigma_T^2 \mathbf{I})$  and iterates via Eq. (3) through numerical discretization to produce a clean sample  $\mathbf{x}_0$ .

**Image-to-Noise Inversion.** Obtaining the initial noise that generates a given real image is a fundamental prerequisite for many applications, making inversion of the sampling process essential. Deterministic sampling methods, particularly DDIM, provide a tractable approach to achieve this goal.

Image interpolation exemplifies a key application of inversion, where the goal is to generate semantically meaningful intermediate frames between two images. Several methods leverage diffusion models to achieve realistic transitions through noise space interpolation (Wang & Golland, 2023; Zhang et al., 2024). A common approach is SLERP (Shoemake, 1985), which interpolates between inverted noise vectors  $\mathbf{x}_T^0$  and  $\mathbf{x}_T^1$  (corresponding to images  $\mathbf{x}_0^0$  and  $\mathbf{x}_0^1$ ) via:

$$\mathbf{x}_T^{\lambda} = \frac{\sin((1-\lambda)\theta)}{\sin \theta} \mathbf{x}_T^0 + \frac{\sin(\lambda\theta)}{\sin \theta} \mathbf{x}_T^1, \quad (4)$$

where  $\lambda \in [0, 1]$  controls interpolation and  $\theta$  is the angle between noise vectors. The interpolated noise  $\mathbf{x}_T^{\lambda}$  is then decoded via forward sampling to generate intermediate frames. Interpolation quality critically depends on the accuracy and Gaussian properties of inverted noise.

The inversion process seeks the noise  $\mathbf{x}_T$  that reconstructs a given image  $\mathbf{x}_0$  through sampling. For DDIM, the discrete sampling process follows:

$$\mathbf{x}_{t_{i-1}} = \phi_{t_i} \mathbf{x}_{t_i} + \psi_{t_i} D_{\theta}(\mathbf{x}_{t_i}, \sigma_{t_i}), \quad (5)$$

where  $\phi_{t_i}$  and  $\psi_{t_i}$  are sampler parameters,  $\{t_i\}$  is a discrete time sequence from 0 to  $T$ , and  $D_{\theta}(\mathbf{x}_{t_i}, \sigma_{t_i})$  denotes the pre-trained denoising network. Directly reversing this process by solving for  $\mathbf{x}_{t_i}$  given  $\mathbf{x}_{t_{i-1}}$  yields an implicit scheme that is computationally inefficient, as  $\mathbf{x}_{t_i}$  appears both directly and within the network evaluation  $D_{\theta}(\mathbf{x}_{t_i}, \sigma_{t_i})$ .

To address this computational challenge, Dhariwal & Nichol (2021) approximate the network output by assuming slow variation along the trajectory:  $D_{\theta}(\mathbf{x}_{t_i}, \sigma_{t_i}) \approx D_{\theta}(\mathbf{x}_{t_{i-1}}, \sigma_{t_i})$ . This yields the DDIM inversion scheme:

$$\mathbf{x}_{t_i} \approx (\mathbf{x}_{t_{i-1}} - \psi_{t_i} D_{\theta}(\mathbf{x}_{t_{i-1}}, \sigma_{t_i})) / \phi_{t_i}. \quad (6)$$

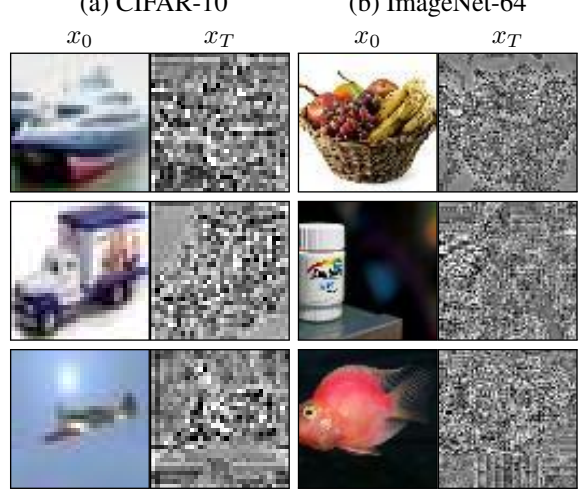


**Figure 2. Inverted noise contains image-dependent patterns.** We visualize a single channel from the inverted noise as grayscale images for two pixel-space models, showing clear correlation with the original images.

However, this approach has notable limitations. It requires many inversion steps to maintain accuracy, which conflicts with few-step diffusion models (Lu et al., 2023; Zhang & Chen, 2023). Moreover, recent studies (Parmar et al., 2023; Garibi et al., 2024; Staniszewski et al., 2024) reveal two critical issues: (1) **unreliable reconstruction** in certain models and scenarios, particularly with classifier-free guidance (Ho & Salimans, 2021); (2) **non-Gaussian inverted noise** as illustrated in Fig. 2, which degrades editability.

## 4. Our Method

In this section, we present a novel approach for addressing inversion failures in diffusion models. We first establish the fundamental causes of inversion inaccuracy through theoretical analysis and experimental validation, identifying two key challenges: the singular behavior of score functions near  $t = 0$  and the ill-posedness of the inversion problem. We then propose *Singularity Skipping Inversion (SSI)*, a method that skips the singular region to achieve stable inversion. Finally, we analyze the tradeoff between reconstruction fidelity and editability.

### 4.1. Singularity and Ill-posedness of Inversion

Prior works have noted that inversion processes generally exhibit inaccuracy. Moreover, Staniszewski et al. (2024) observes that such errors concentrate in the early inversion steps (i.e., when  $t$  is close to 0), leading to non-Gaussian characteristics of inverted noise and unreliable reconstruction. To understand the root cause of this phenomenon, we investigate the behavior of score functions during inversion.

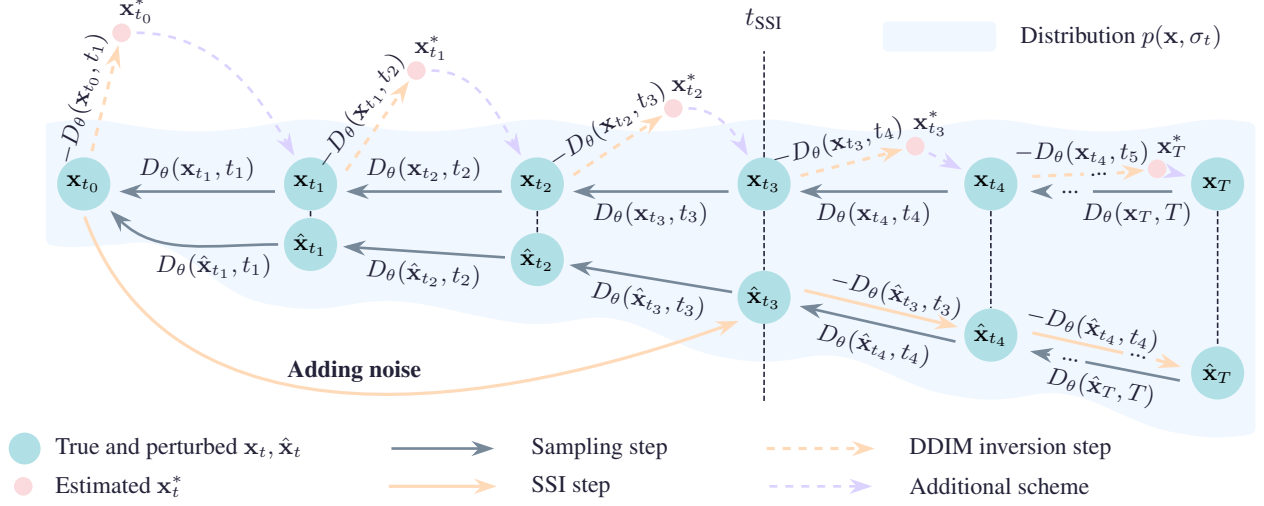
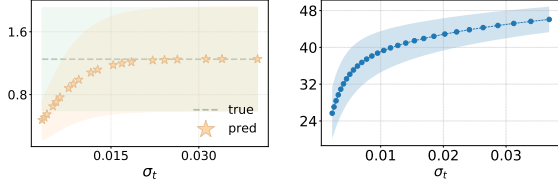


Figure 3. SSI method overview: Starting from a clean image  $\mathbf{x}_0$  and adding noise to this image, we sample  $\hat{\mathbf{x}}_{t_{\text{SSI}}} \sim p(\mathbf{x}; \sigma_{t_{\text{SSI}}})$  at an early time  $t_{\text{SSI}}$  to bypass the singularity near  $t = 0$ , then iteratively solve the reverse ODE through an alternative trajectory to obtain  $\hat{\mathbf{x}}_T$ . Different noise samples allow distinct paths that faithfully reconstruct  $\mathbf{x}_0$ . By avoiding ill-conditioned early-time steps, SSI generates high quality and editable Gaussian noises and reduces computational costs compared to methods requiring extra corrections.

#### Observation 1: Singular behavior of score functions.

Along sampling trajectories, the score function diverges at the rate of  $1/\sigma_t$  as  $t \rightarrow 0$ .



(a) Point cloud distribution (b) Pretrained EDM model

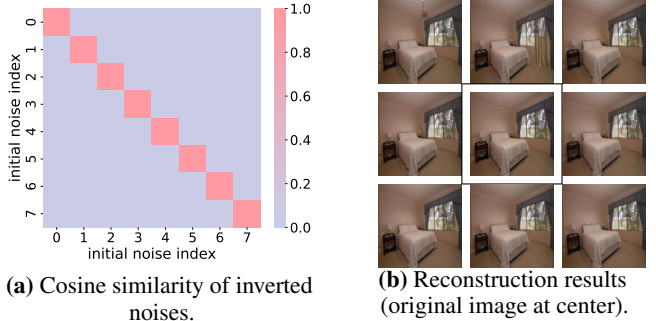
Figure 4. Visualization of  $\|\mathbb{E}[\mathbf{x}_0|\mathbf{x}_t] - \mathbf{x}_t\|/\sigma_t$  along sampling trajectories. For distributions with analytically computable score functions (Fig. 4a), the true score function exhibits  $1/\sigma_t$  divergence as  $t \rightarrow 0$ , while neural network approximations show significant relative errors in this regime. Pretrained image diffusion models on CIFAR-10 (Fig. 4b) demonstrate the same characteristic behavior.

Fig. 4 illustrates this observation along sampling trajectories. This singular behavior implies that near  $t = 0$ , neural network approximation errors are further amplified, leading to inaccurate inversion results. We provide the theoretical explanation of this singularity in Appendix A.

#### Observation 2: Ill-posedness of inversion.

Multiple nearly orthogonal initial noise vectors can generate samples that are very close to the real image, indicating that the inversion process is ill-posed.

Fig. 5 demonstrates this ill-posedness empirically. As shown in Fig. 5a, inverted noise vectors exhibit low cosine simi-



(a) Cosine similarity of inverted noises.  
(b) Reconstruction results (original image at center).

Figure 5. Cosine similarity between different inverted noise vectors (SSI-DM) and reconstruction results.

larity despite producing similar reconstructions (Fig. 5b). This reveals that multiple nearly orthogonal initial noise vectors can generate visually similar images, indicating that the inversion problem admits *multiple valid solutions* and is sensitive to input images.

These observations motivate our algorithmic design. The inversion process should yield Gaussian noise with editing capabilities, yet accurately inverting along the original generation trajectory is extremely challenging due to the ill-posed nature of the problem. Rather than pursuing highly precise numerical schemes for trajectory inversion, we adopt a pragmatic approach: obtaining *any* valid noise vector that faithfully reconstructs the real image while ensuring the invertibility and editability of the initial noise representation.

## 4.2. Singularity Skipping Inversion (SSI)

**Key insight:** Rather than inverting through the singular region where approximation errors accumulate, we exploit the explicit tractability of forward diffusion to directly sample at an intermediate time point  $t_{\text{SSI}} > 0$ . This bypasses the singular region, allowing stable inversion from  $t_{\text{SSI}}$  to  $T$  that yields editable Gaussian noise.

Our method consists of two steps:

**Step 1:** Obtain a sample from the marginal distribution  $p(\mathbf{x}; \sigma_{t_{\text{SSI}}})$  at the designated “skipping time”  $t_{\text{SSI}}$  by directly adding independent Gaussian noise to the clean image.

**Step 2:** Perform inversion from  $t_{\text{SSI}}$  to  $T$  using standard numerical integration of the reverse ODE. Starting inversion from  $t_{\text{SSI}}$  avoids the singular region near  $t = 0$ .

**Algorithm.** For the sampling ODE (3), our method proceeds as follows. Given a real image  $\mathbf{x}_0$ , we first obtain a sample from the marginal distribution  $p(\mathbf{x}; \sigma_{t_{\text{SSI}}})$  at time  $t_{\text{SSI}}$  by adding independent Gaussian noise to  $\mathbf{x}_0$ :

$$\mathbf{x}_{t_{\text{SSI}}} = \mathbf{x}_0 + \sigma_{t_{\text{SSI}}} \mathbf{n}, \quad \mathbf{n} \sim \mathcal{N}(\mathbf{0}, \mathbf{I}), \quad (7)$$

which transitions to an intermediate point on an alternative sampling trajectory. Subsequently, we perform numerical integration of the reverse ODE from  $t_{\text{SSI}}$  to  $T$  using standard discretization schemes, e.g., Euler’s method. At each discretization step from  $\tau_i$  to  $\tau_{i+1}$  with  $\tau_0 = t_{\text{SSI}}$  and  $\tau_N = T$ , we compute:

$$\mathbf{x}_{\tau_{i+1}} = \mathbf{x}_{\tau_i} - \dot{\sigma}_{\tau_i} \sigma_{\tau_i} \nabla_{\mathbf{x}} \log p(\mathbf{x}_{\tau_i}; \sigma_{\tau_i}) (\tau_{i+1} - \tau_i), \quad (8)$$

where the score function  $\nabla_{\mathbf{x}} \log p(\mathbf{x}_{\tau_i}; \sigma_{\tau_i})$  is approximated via the pretrained denoising network  $D_{\theta}$  as  $(D_{\theta}(\mathbf{x}_{\tau_i}, \sigma_{\tau_i}) - \mathbf{x}_{\tau_i})/\sigma_{\tau_i}^2$ . The complete algorithmic specification for VE processes is formalized in Algorithm 1. We note that while the algorithm is presented here for VE processes, the framework naturally generalizes to VP processes (e.g., DDIM), as detailed in the Appendix B.

## 4.3. Reconstruction Fidelity and Editability Tradeoff

The goal of the inversion process is to obtain an initial noise representation that can accurately reconstruct the original image while possessing Gaussian properties that enable effective editing and interpolation. However, achieving both objectives simultaneously presents a fundamental tradeoff, which we analyze below.

**Reconstruction error bound.** To evaluate our inversion method, we first examine whether samples generated from the perturbed trajectory that SSI jumps to remain sufficiently close to the input image. Following Meng et al. (2022), for VE processes Eq. (3), we establish that the reconstruction error is bounded by  $\sigma_{t_{\text{SSI}}}$ :

**Algorithm 1** Singularity Skipping Inversion (for VE processes with Euler method)

**Require:** clean image  $\mathbf{x}_0$ , skipping time  $t_{\text{SSI}}$ , final time  $T$ , time steps  $\{\tau_i\}_{i=0}^N$  with  $\tau_0 = t_{\text{SSI}}$ ,  $\tau_N = T$ , pretrained neural network  $D_{\theta}$

**Ensure:** A noisy latent  $\mathbf{x}_T$

- 1: Sample  $\mathbf{n} \sim \mathcal{N}(\mathbf{0}, \mathbf{I})$
- 2:  $\mathbf{x}_{\tau_0} \leftarrow \mathbf{x}_0 + \sigma_{\tau_0} \mathbf{n}$
- 3: **for**  $i = 0, 1, \dots, N - 1$  **do**
- 4:    $\nabla_{\mathbf{x}} \log p(\mathbf{x}_{\tau_i}; \sigma_{\tau_i}) \leftarrow (D_{\theta}(\mathbf{x}_{\tau_i}, \sigma_{\tau_i}) - \mathbf{x}_{\tau_i})/\sigma_{\tau_i}^2$
- 5:    $\mathbf{x}_{\tau_{i+1}} \leftarrow \mathbf{x}_{\tau_i} - \dot{\sigma}_{\tau_i} \sigma_{\tau_i} \nabla_{\mathbf{x}} \log p(\mathbf{x}_{\tau_i}; \sigma_{\tau_i}) (\tau_{i+1} - \tau_i)$
- 6: **end for**
- 7:  $\mathbf{x}_T \leftarrow \mathbf{x}_{\tau_N}$

**Proposition 4.1.** Assume that  $\|\nabla_{\mathbf{x}} \log p(\mathbf{x}_t; \sigma_t)\|_2 \leq C/\sigma_t$  for all  $\mathbf{x}_t$  along the sampling trajectory and  $t \in [t_{\text{SSI}}, T]$ . Then for all  $\delta \in (0, 1)$ , with probability at least  $1 - \delta$ , the reconstruction error satisfies

$$\left\| \frac{\mathbf{x}_0 - \hat{\mathbf{x}}_0}{\sigma_{t_{\text{SSI}}}} \right\|_2 \leq C + \sqrt{d + 2\sqrt{-d \log \delta} - 2 \log \delta}, \quad (9)$$

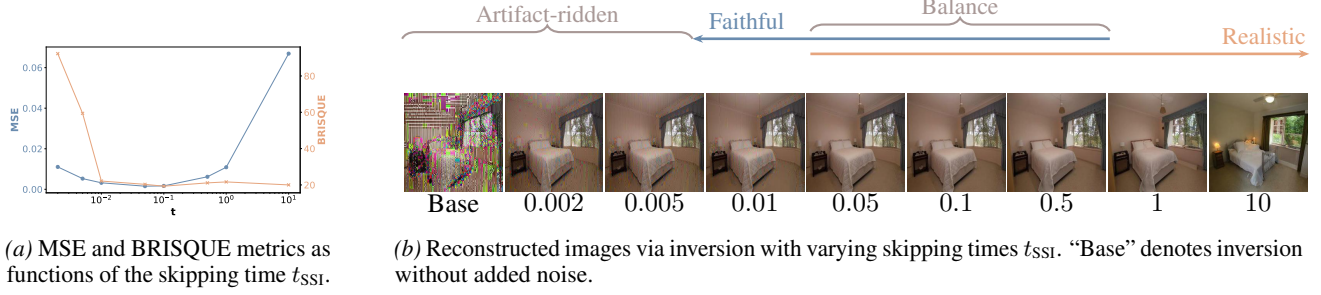
where  $d$  is the dimension of the image space and  $\hat{\mathbf{x}}_0$  denotes the image sampled from the perturbed trajectory that SSI jumps to.

The proof is provided in Appendix A. Proposition 4.1 establishes that the ideal reconstruction error is directly controlled by  $\sigma_{t_{\text{SSI}}}$ , providing a theoretical foundation for understanding this tradeoff.

Fig. 6 provides empirical validation of this tradeoff. As  $t_{\text{SSI}}$  increases, the singular region near  $t = 0$  is progressively skipped, making the inversion process gradually stable. This stability enables the generation of realistic images, and sufficient realism is achieved once  $t_{\text{SSI}}$  exceeds a modest threshold, as visually demonstrated in Fig. 6b.

On the other hand, when  $t_{\text{SSI}}$  is extremely small, inversion inaccuracies lead to poor reconstruction quality with visible artifacts. This reconstruction error decreases rapidly as  $t_{\text{SSI}}$  increases, as evidenced by the sharp drop in MSE and BRISQUE metrics in Fig. 6a. As  $t_{\text{SSI}}$  continues to grow, the perturbed trajectory increasingly deviates from the original image. While the inverted noise still generates high-quality samples, these samples progressively diverge from the original image, as demonstrated by the gradual increase in reconstruction error for larger  $t_{\text{SSI}}$  values in Fig. 6a and the visual progression in Fig. 6b.

**Practical balance.** This analysis reveals that selecting an intermediate  $t_{\text{SSI}}$  value achieves a practical balance between reconstruction fidelity and image realism. As demonstrated in Fig. 6, choosing  $t_{\text{SSI}}$  within an appropriate range (e.g., for EDM  $t_{\text{SSI}} \in [0.05, 0.5]$ ) ensures both realistic image



(a) MSE and BRISQUE metrics as functions of the skipping time  $t_{\text{SSI}}$ .

(b) Reconstructed images via inversion with varying skipping times  $t_{\text{SSI}}$ . “Base” denotes inversion without added noise.

Figure 6. Trade-off between faithfulness and realism in image reconstruction. When the skipping time  $t_{\text{SSI}}$  is too small, reconstructed images exhibit significant artifacts and poor quality. As  $t_{\text{SSI}}$  increases beyond a certain threshold, image quality improves dramatically, achieving close alignment with the original. However, further increasing  $t_{\text{SSI}}$  causes reconstructed images to gradually diverge from the original.

generation and faithful reconstruction, effectively avoiding the artifact-ridden results from excessively small  $t_{\text{SSI}}$  values and the substantial deviation from the original image at overly large  $t_{\text{SSI}}$  values.

## 5. Experiments

In this section, we evaluate SSI across two diffusion frameworks—DDIM and EDM—on multiple benchmarks: LSUN Bedroom-256 and ImageNet-256. We conduct three primary experiments: *image inversion*, *image reconstruction*, and *image interpolation*, demonstrating SSI’s plug-and-play compatibility and effectiveness. All models used in our experiments are pretrained from prior works (Song et al., 2023; Dhariwal & Nichol, 2021):

- DDIM on 256x256 diffusion (not class conditional): [https://openaipublic.blob.core.windows.net/diffusion/jul-2021/256x256\\_diffusion\\_uncond.pt](https://openaipublic.blob.core.windows.net/diffusion/jul-2021/256x256_diffusion_uncond.pt)
- DDIM on LSUN bedroom: [https://openaipublic.blob.core.windows.net/diffusion/jul-2021/lsun\\_bedroom.pt](https://openaipublic.blob.core.windows.net/diffusion/jul-2021/lsun_bedroom.pt)
- DDIM on LSUN cat: [https://openaipublic.blob.core.windows.net/diffusion/jul-2021/lsun\\_cat.pt](https://openaipublic.blob.core.windows.net/diffusion/jul-2021/lsun_cat.pt)
- EDM on LSUN Bedroom-256: [https://openaipublic.blob.core.windows.net/consistency/edm\\_bedroom256\\_ema.pt](https://openaipublic.blob.core.windows.net/consistency/edm_bedroom256_ema.pt)
- EDM on LSUN Cat-256: [https://openaipublic.blob.core.windows.net/consistency/edm\\_cat256\\_ema.pt](https://openaipublic.blob.core.windows.net/consistency/edm_cat256_ema.pt)

### 5.1. Experiment settings

**DDIM:** We follow the configurations from Song et al. (2021a): the forward process consists of 1000 timesteps. To accelerate sampling, we select a subsequence  $\kappa \subset \{1, 2, \dots, 1000\}$  as the actual discrete timesteps for our experiments.

**EDM:** We set  $s(t) = 1$ ,  $\sigma(t) = t$ , and define the timestep size using the following formula:

$$t_{i>0} = \left( t_{\min}^{1/\rho} + \frac{i-1}{N-1} (t_{\max}^{1/\rho} - t_{\min}^{1/\rho}) \right)^\rho, t_0 = 0, \quad (10)$$

where  $\rho = 7.0$  and  $t_{\max} = 80$ ,  $t_{\min} = 0.002$ ,  $N = 200$ . In the subsequence experiments, we use forward Euler method to discrete the ODE (3).

**Baselines.** For comparative experiments, we adopt the following base methods: for DDIM, we use the inversion method proposed in Dhariwal & Nichol (2021); for EDM, we employ the forward Euler method to solve ODE (3) without applying SSI.

All diffusion models used in our experiments are *third-party pretrained checkpoints* released by prior work; we do *not* perform any additional training, fine-tuning, or distillation.

### 5.2. LSUN Bedroom-256

**Image Inversion.** For DDIM, we use timesteps  $\kappa = [1, 3, \dots, 999]$  and add noise up to  $\kappa_{20} = 39$  before inversion. For EDM, we add noise up to  $t_{\text{SSI}} = 0.1$  before inversion. We randomly select 300 images from the LSUN Bedroom-256 test set and invert them into the noise space using both SSI and the base method. Partial results are shown in Fig. 7. We compute inter-channel, horizontal, and vertical correlations of the inverted noise to quantify its Gaussian properties. Results are presented in Table 1.

As shown in Fig. 7, the base method produces noise exhibiting noticeable structural and block-like patterns, indicating strong local correlations and residual image textures. In contrast, SSI yields noise that is visually more homogeneous and closely resembles random Gaussian noise. This observation is quantitatively confirmed in Table 1, where SSI consistently achieves significantly lower correlation values across all metrics.

**Image Reconstruction.** Using the inverted noise obtained

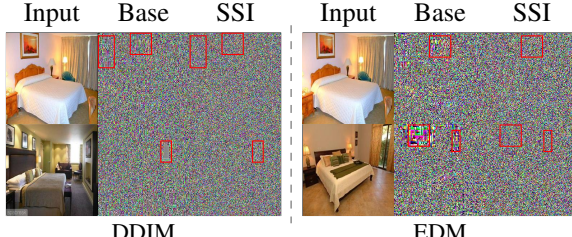


Figure 7. Inversions on LSUN Bedroom-256



Figure 8. Reconstructions on LSUN Bedroom-256

above, we apply the full sampling process to reconstruct images, as shown in Fig. 8. Quantitative results in Table 1 report average MSE, LPIPS, and SSIM metrics between original and reconstructed images.

SSI achieves substantially better reconstruction quality than the base method, effectively mitigating color distortion artifacts. This improvement is consistently reflected across all quantitative metrics.

**Image Interpolation.** Building on the successful reconstruction results, we evaluate SSI on image interpolation tasks. Given two inverted noise vectors, we apply SLERP Eq. (4) to generate intermediate noise states. We test with interpolation coefficients  $\lambda \in \{0.1, 0.3, 0.5, 0.7, 0.9\}$ . Results are shown in Fig. 12.

The base method frequently produces interpolated images with unrealistic artifacts and visual inconsistencies, whereas SSI significantly improves interpolation quality while maintaining smooth visual coherence throughout the sequence. To quantitatively evaluate interpolation quality, we compute the Fréchet Inception Distance (FID) (Heusel et al., 2017) between 5,000 training images and the following sets: 500 interpolated images for each  $\lambda$ , and a baseline of 500 images sampled directly from Gaussian noise using the diffusion model. Results are presented in Fig. 11. SSI achieves substantially lower FID scores than the base method, with interpolation quality closely approaching that of direct sampling from Gaussian noise.

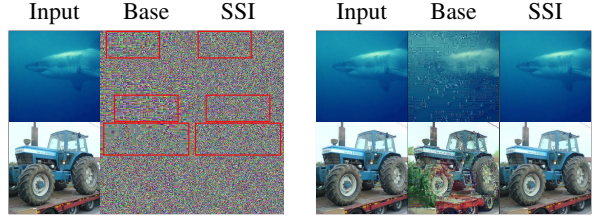


Figure 9. Inversions of DDIM on ImageNet-256

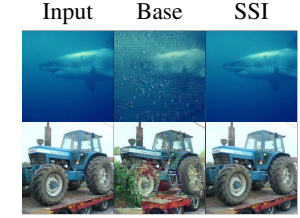


Figure 10. Reconstructions of DDIM on ImageNet-256

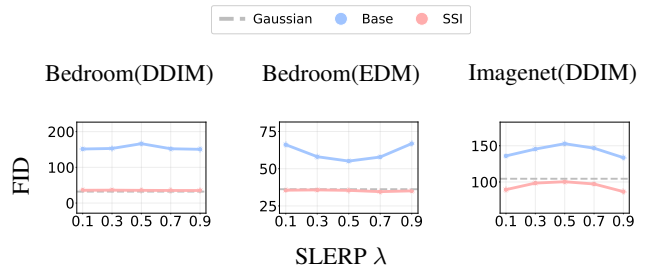


Figure 11. FID of interpolations. The dashed line represents sampling using the diffusion model starting from Gaussian noise.

### 5.3. ImageNet-256

To evaluate SSI on more complex and diverse data, we randomly select images from multiple classes in the ImageNet-256 dataset. We test DDIM without class conditioning, using timesteps  $\kappa = [1, 3, \dots, 999]$  and adding noise up to  $\kappa_2 = 3$ . All other settings follow those used for DDIM on LSUN Bedroom-256. **Image Inversion.** We select 300 images from different classes, invert them into the noise space, and compute inter-channel, horizontal, and vertical correlations. Results are shown in Fig. 9 and Table 1.

**Image Reconstruction.** Using the inverted noise from above, we apply the full sampling process to reconstruct images. Quantitative metrics are reported in Fig. 10 and Table 1.

**Image Interpolation.** We perform interpolation on multiple

Table 1. Inversion metrics and reconstruction quality metrics for different datasets and methods.

		Inversion			Reconstruction		
		CHAN↓	HORI↓	VERT↓	MSE↓	LPIPS↓	SSIM↑
LSUN Bedroom-256							
DDIM	Base	0.047	0.134	0.136	0.177	0.606	0.289
	<b>SSI</b>	<b>0.002</b>	<b>0.050</b>	<b>0.050</b>	<b>0.006</b>	<b>0.135</b>	<b>0.879</b>
	Gaussian	0.003	0.050	0.050	-	-	-
EDM	Base	0.108	0.139	0.122	0.025	0.365	0.639
	<b>SSI</b>	<b>0.004</b>	<b>0.050</b>	<b>0.050</b>	<b>0.009</b>	<b>0.170</b>	<b>0.859</b>
	Gaussian	0.003	0.050	0.050	-	-	-
ImageNet-256							
DDIM	Base	0.044	0.108	0.092	0.072	0.398	0.541
	<b>SSI</b>	<b>0.004</b>	<b>0.052</b>	<b>0.052</b>	<b>0.002</b>	<b>0.050</b>	<b>0.967</b>
	Gaussian	0.003	0.050	0.050	-	-	-

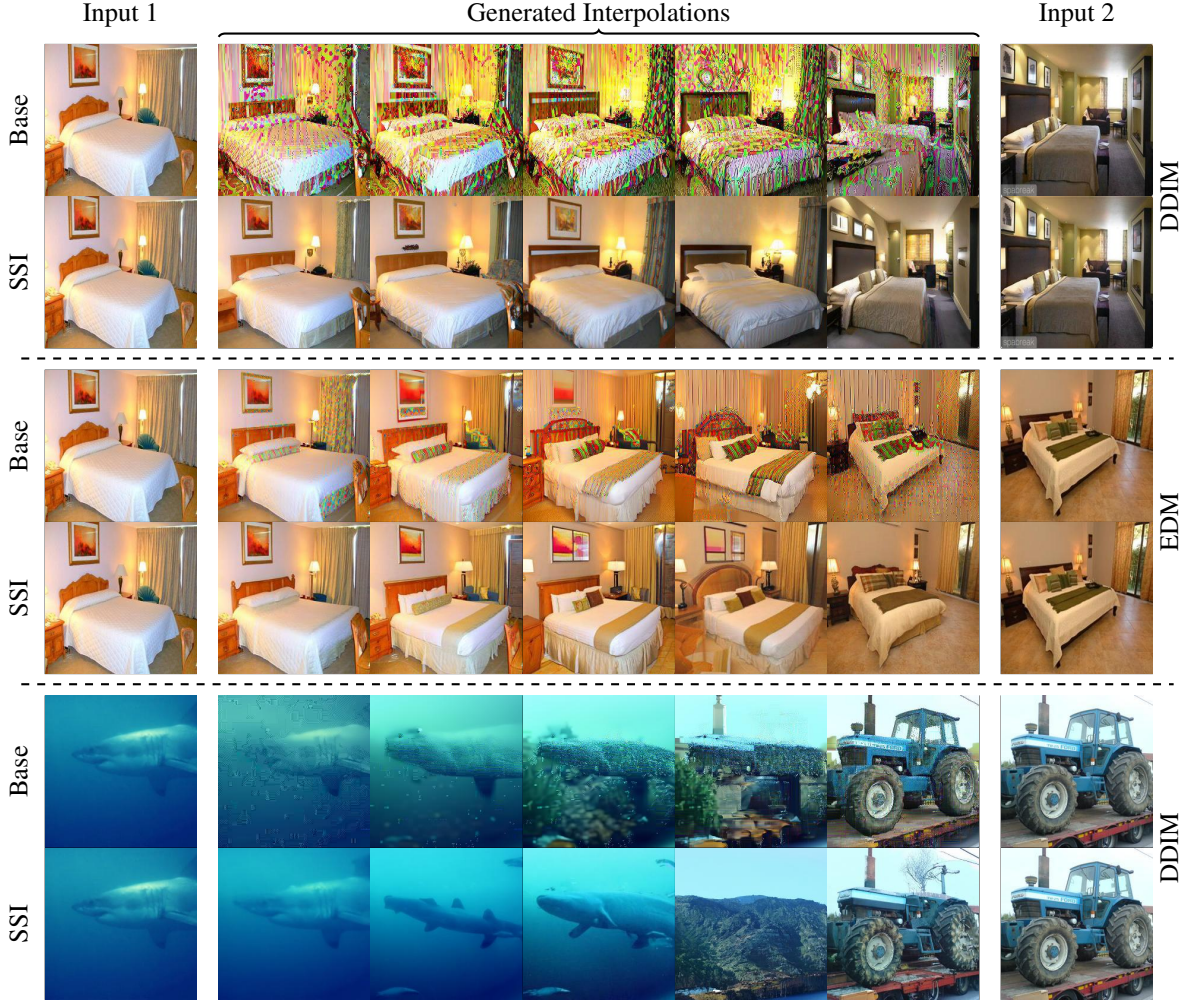


Figure 12. Interpolation results. The first 4 rows are on LSUN Bedroom-256 using DDIM and EDM, while the last 2 rows are on ImageNet-256 using DDIM. Interpolation coefficients  $\lambda$  are  $[0.1, 0.3, 0.5, 0.7, 0.9]$ .

image pairs and compute FID scores between interpolated images, training images, and samples from Gaussian noise. Interpolation results are shown in Fig. 12 and FID scores in Fig. 11.

On the more complex ImageNet-256 dataset, SSI significantly outperforms the base method both visually and quantitatively across all three tasks—involution, reconstruction, and interpolation. This demonstrates SSI’s effectiveness on diverse, multi-class datasets.

## 6. Conclusion

In this paper, we analyze the singularity at  $t = 0$  in the general diffusion framework and propose Singularity Skipping Inversion, an inversion method for deterministic generative processes that effectively bypasses this singularity. Our method produces inverted noise that more closely approximates Gaussian distributions, leading to improved perfor-

mance in downstream tasks. The theoretical foundation of our approach ensures high interpretability and broad applicability across different generative frameworks and datasets.

**Limitations and future work.** Our theoretical analysis currently focuses on unconditional pixel-space diffusion models. While we have empirically validated the effectiveness of our method on latent diffusion models such as Stable Diffusion, a rigorous theoretical understanding of how VAE encoding and Classifier-Free Guidance affect inversion quality remains an open question. Furthermore, our method’s plug-and-play nature suggests promising applications to other image editing tasks, including prompt-based editing and style transfer, which we leave for future investigation.

## Impact Statement

This paper presents work whose goal is to advance the field of Machine Learning. There are many potential societal

consequences of our work, none which we feel must be specifically highlighted here.

## References

Anderson, B. D. Reverse-time diffusion equation models. *Stochastic Processes and their Applications*, 12(3):313–326, 1982.

Bortoli, V. D. Convergence of denoising diffusion models under the manifold hypothesis. *Transactions on Machine Learning Research*, 2022. ISSN 2835-8856. URL <https://openreview.net/forum?id=MhK5aXo3gB>. Expert Certification.

Brack, M., Friedrich, F., Kornmeier, K., Tsaban, L., Schramowski, P., Kersting, K., and Passos, A. Ledit++: Limitless image editing using text-to-image models. In *Proceedings of the IEEE/CVF conference on computer vision and pattern recognition*, pp. 8861–8870, 2024.

Brooks, T., Holynski, A., and Efros, A. A. Instructpix2pix: Learning to follow image editing instructions. In *Proceedings of the IEEE/CVF conference on computer vision and pattern recognition*, pp. 18392–18402, 2023.

Chen, H., Lee, H., and Lu, J. Improved analysis of score-based generative modeling: User-friendly bounds under minimal smoothness assumptions. In *International Conference on Machine Learning*, pp. 4735–4763. PMLR, 2023a.

Chen, M., Huang, K., Zhao, T., and Wang, M. Score approximation, estimation and distribution recovery of diffusion models on low-dimensional data. In *International Conference on Machine Learning*, pp. 4672–4712. PMLR, 2023b.

Chen, S., Chewi, S., Li, J., Li, Y., Salim, A., and Zhang, A. Sampling is as easy as learning the score: theory for diffusion models with minimal data assumptions. In *The Eleventh International Conference on Learning Representations*, 2023c. URL [https://openreview.net/forum?id=zyLVMgsZ0U\\_](https://openreview.net/forum?id=zyLVMgsZ0U_).

Cho, H., Lee, J., Kim, S. B., Oh, T.-H., and Jeong, Y. Noise map guidance: Inversion with spatial context for real image editing. In *The Twelfth International Conference on Learning Representations*, 2024. URL <https://openreview.net/forum?id=mhgm0IXtHw>.

Dhariwal, P. and Nichol, A. Q. Diffusion models beat GANs on image synthesis. In Beygelzimer, A., Dauphin, Y., Liang, P., and Vaughan, J. W. (eds.), *Advances in Neural Information Processing Systems*, 2021. URL <https://openreview.net/forum?id=AAWuCvzaVt>.

Dong, W., Xue, S., Duan, X., and Han, S. Prompt tuning inversion for text-driven image editing using diffusion models. In *Proceedings of the IEEE/CVF International Conference on Computer Vision*, pp. 7430–7440, 2023.

Garibi, D., Patashnik, O., Voynov, A., Averbuch-Elor, H., and Cohen-Or, D. Renoise: Real image inversion through iterative noising. In *European Conference on Computer Vision*, pp. 395–413. Springer, 2024.

Goodfellow, I. J., Pouget-Abadie, J., Mirza, M., Xu, B., Warde-Farley, D., Ozair, S., Courville, A., and Bengio, Y. Generative adversarial nets. *Advances in neural information processing systems*, 27, 2014.

Han, L., Wen, S., Chen, Q., Zhang, Z., Song, K., Ren, M., Gao, R., Stathopoulos, A., He, X., Chen, Y., Liu, D., Zhangli, Q., Jiang, J., Xia, Z., Srivastava, A., and Metaxas, D. Proxedit: Improving tuning-free real image editing with proximal guidance. In *2024 IEEE/CVF Winter Conference on Applications of Computer Vision (WACV)*, pp. 4279–4289, 2024. doi: 10.1109/WACV57701.2024.00424.

Hertz, A., Mokady, R., Tenenbaum, J., Aberman, K., Pritch, Y., and Cohen-Or, D. Prompt-to-prompt image editing with cross-attention control. In *The Eleventh International Conference on Learning Representations*, 2023. URL [https://openreview.net/forum?id=\\_CDixzkzeyb](https://openreview.net/forum?id=_CDixzkzeyb).

Heusel, M., Ramsauer, H., Unterthiner, T., Nessler, B., and Hochreiter, S. Gans trained by a two time-scale update rule converge to a local nash equilibrium. *Advances in neural information processing systems*, 30, 2017.

Ho, J. and Salimans, T. Classifier-free diffusion guidance. In *NeurIPS 2021 Workshop on Deep Generative Models and Downstream Applications*, 2021. URL <https://openreview.net/forum?id=qw8AKxfYbI>.

Ho, J., Jain, A., and Abbeel, P. Denoising diffusion probabilistic models. *Advances in neural information processing systems*, 33:6840–6851, 2020.

Huberman-Spiegelglas, I., Kulikov, V., and Michaeli, T. An edit friendly ddpm noise space: Inversion and manipulations. In *Proceedings of the IEEE/CVF Conference on Computer Vision and Pattern Recognition*, pp. 12469–12478, 2024.

Karras, T., Aittala, M., Aila, T., and Laine, S. Elucidating the design space of diffusion-based generative models. In Oh, A. H., Agarwal, A., Belgrave, D., and Cho, K. (eds.), *Advances in Neural Information Processing Systems*, 2022. URL <https://openreview.net/forum?id=k7FuTOWMOc7>.

Kawar, B., Zada, S., Lang, O., Tov, O., Chang, H., Dekel, T., Mosseri, I., and Irani, M. Imagic: Text-based real image editing with diffusion models. In *Proceedings of the IEEE/CVF conference on computer vision and pattern recognition*, pp. 6007–6017, 2023.

Kim, G., Kwon, T., and Ye, J. C. Diffusionclip: Text-guided diffusion models for robust image manipulation. In *Proceedings of the IEEE/CVF conference on computer vision and pattern recognition*, pp. 2426–2435, 2022.

Kingma, D. P. and Welling, M. Auto-encoding variational bayes. *arXiv preprint arXiv:1312.6114*, 2013.

Laurent, B. and Massart, P. Adaptive estimation of a quadratic functional by model selection. *Annals of statistics*, pp. 1302–1338, 2000.

Lin, H., Chen, Y., Wang, J., An, W., Wang, M., Tian, F., Liu, Y., Dai, G., Wang, J., and Wang, Q. Schedule your edit: A simple yet effective diffusion noise schedule for image editing. In *The Thirty-eighth Annual Conference on Neural Information Processing Systems*, 2024. URL <https://openreview.net/forum?id=Yu6cDt7q9Z>.

Liu, Z., Zhang, W., and Li, T. Improving the euclidean diffusion generation of manifold data by mitigating score function singularity. In *The Thirty-ninth Annual Conference on Neural Information Processing Systems*, 2025. URL <https://openreview.net/forum?id=T98sh6P0Vm>.

Lu, Y., Wang, Z., and Bal, G. Mathematical analysis of singularities in the diffusion model under the submanifold assumption. *arXiv preprint arXiv:2301.07882*, 2023.

Meng, C., He, Y., Song, Y., Song, J., Wu, J., Zhu, J.-Y., and Ermon, S. SDEdit: Guided image synthesis and editing with stochastic differential equations. In *International Conference on Learning Representations*, 2022. URL [https://openreview.net/forum?id=aBsCjcPu\\_tE](https://openreview.net/forum?id=aBsCjcPu_tE).

Miyake, D., Iohara, A., Saito, Y., and Tanaka, T. Negative-prompt inversion: Fast image inversion for editing with text-guided diffusion models. In *2025 IEEE/CVF Winter Conference on Applications of Computer Vision (WACV)*, pp. 2063–2072. IEEE, 2025.

Mokady, R., Hertz, A., Aberman, K., Pritch, Y., and Cohen-Or, D. Null-text inversion for editing real images using guided diffusion models. In *Proceedings of the IEEE/CVF conference on computer vision and pattern recognition*, pp. 6038–6047, 2023.

Parmar, G., Kumar Singh, K., Zhang, R., Li, Y., Lu, J., and Zhu, J.-Y. Zero-shot image-to-image translation. In *ACM SIGGRAPH 2023 conference proceedings*, pp. 1–11, 2023.

Pidstrigach, J. Score-based generative models detect manifolds. In Oh, A. H., Agarwal, A., Belgrave, D., and Cho, K. (eds.), *Advances in Neural Information Processing Systems*, 2022. URL <https://openreview.net/forum?id=AiNrnIrDfD9>.

Rombach, R., Blattmann, A., Lorenz, D., Esser, P., and Ommer, B. High-resolution image synthesis with latent diffusion models. In *Proceedings of the IEEE/CVF conference on computer vision and pattern recognition*, pp. 10684–10695, 2022.

Saharia, C., Chan, W., Saxena, S., Li, L., Whang, J., Denton, E. L., Ghasemipour, K., Gontijo Lopes, R., Karagol Ayan, B., Salimans, T., et al. Photorealistic text-to-image diffusion models with deep language understanding. *Advances in neural information processing systems*, 35: 36479–36494, 2022.

Shoemake, K. Animating rotation with quaternion curves. *Proceedings of the 12th annual conference on Computer graphics and interactive techniques*, 1985. URL <https://api.semanticscholar.org/CorpusID:11290566>.

Song, J., Meng, C., and Ermon, S. Denoising diffusion implicit models. In *International Conference on Learning Representations*, 2021a. URL <https://openreview.net/forum?id=St1giarCHLP>.

Song, Y., Sohl-Dickstein, J., Kingma, D. P., Kumar, A., Ermon, S., and Poole, B. Score-based generative modeling through stochastic differential equations. In *International Conference on Learning Representations*, 2021b. URL <https://openreview.net/forum?id=PxTIG12RRHS>.

Song, Y., Dhariwal, P., Chen, M., and Sutskever, I. Consistency models. In *Proceedings of the 40th International Conference on Machine Learning*, pp. 32211–32252, 2023.

Staniszewski, Ł., Kuciński, Ł., and Deja, K. There and back again: On the relation between noise and image inversions in diffusion models. *arXiv preprint arXiv:2410.23530*, 2024.

Stéphanovitch, A. Regularity of the score function in generative models. *arXiv preprint arXiv:2506.19559*, 2025.

Tumanyan, N., Geyer, M., Bagon, S., and Dekel, T. Plug-and-play diffusion features for text-driven image-to-image translation. In *Proceedings of the IEEE/CVF conference on computer vision and pattern recognition*, pp. 1921–1930, 2023.

Vershynin, R. *High-dimensional probability: An introduction with applications in data science*, volume 47. Cambridge university press, 2018.

Wallace, B., Gokul, A., and Naik, N. Edict: Exact diffusion inversion via coupled transformations. In *Proceedings of the IEEE/CVF Conference on Computer Vision and Pattern Recognition*, pp. 22532–22541, 2023.

Wang, C. J. and Golland, P. Interpolating between images with diffusion models, 2023.

Zhang, G., Ji, J., Zhang, Y., Yu, M., Jaakkola, T., and Chang, S. Towards coherent image inpainting using denoising diffusion implicit models. In *Proceedings of the 40th International Conference on Machine Learning*, pp. 41164–41193, 2023.

Zhang, K., Zhou, Y., Xu, X., Dai, B., and Pan, X. Diffmorpher: Unleashing the capability of diffusion models for image morphing. In *Proceedings of the IEEE/CVF Conference on Computer Vision and Pattern Recognition*, pp. 7912–7921, 2024.

Zhang, Q. and Chen, Y. Fast sampling of diffusion models with exponential integrator. In *The Eleventh International Conference on Learning Representations*, 2023. URL <https://openreview.net/forum?id=Loek7hfb46P>.

## A. Theoretical Analysis and Proofs

### A.1. Proof of Proposition 4.1

*Proof.* Let  $\hat{\mathbf{x}}_t$  be the solution of the probability flow ODE (3) satisfying the initial condition  $\hat{\mathbf{x}}_{t_{\text{SSI}}} = \mathbf{x}_0 + \sigma_{t_{\text{SSI}}} \mathbf{n}$ , where  $\mathbf{n} \sim \mathcal{N}(\mathbf{0}, \mathbf{I})$ . For VE processes, the probability flow ODE reads

$$\frac{d\hat{\mathbf{x}}_t}{dt} = -\dot{\sigma}_t \sigma_t \nabla_{\mathbf{x}} \log p(\hat{\mathbf{x}}_t; \sigma_t).$$

The reconstruction error can be expressed as

$$\|\mathbf{x}_0 - \hat{\mathbf{x}}_0\|_2 = \left\| \mathbf{x}_0 - \left( \hat{\mathbf{x}}_{t_{\text{SSI}}} + \int_{t_{\text{SSI}}}^0 \frac{d\hat{\mathbf{x}}_t}{dt} dt \right) \right\|_2 = \left\| -\sigma_{t_{\text{SSI}}} \mathbf{n} + \int_{t_{\text{SSI}}}^0 -\dot{\sigma}_t \sigma_t \nabla_{\mathbf{x}} \log p(\hat{\mathbf{x}}_t; \sigma_t) dt \right\|_2.$$

By the triangle inequality,

$$\|\mathbf{x}_0 - \hat{\mathbf{x}}_0\|_2 \leq \left\| \int_{t_{\text{SSI}}}^0 -\dot{\sigma}_t \sigma_t \nabla_{\mathbf{x}} \log p(\hat{\mathbf{x}}_t; \sigma_t) dt \right\|_2 + \|\sigma_{t_{\text{SSI}}} \mathbf{n}\|_2.$$

For the first term, using the assumption  $\|\nabla_{\mathbf{x}} \log p(\mathbf{x}_t; \sigma_t)\| \leq C/\sigma_t$  and the fact that  $\dot{\sigma}_t \geq 0$  (since  $\sigma_t$  is increasing), we have

$$\left\| \int_{t_{\text{SSI}}}^0 -\dot{\sigma}_t \sigma_t \nabla_{\mathbf{x}} \log p(\hat{\mathbf{x}}_t; \sigma_t) dt \right\|_2 \leq \int_0^{t_{\text{SSI}}} \dot{\sigma}_t \sigma_t \|\nabla_{\mathbf{x}} \log p(\hat{\mathbf{x}}_t; \sigma_t)\|_2 dt \leq \int_0^{t_{\text{SSI}}} \dot{\sigma}_t \sigma_t \cdot \frac{C}{\sigma_t} dt = C \int_0^{t_{\text{SSI}}} \dot{\sigma}_t dt.$$

Since  $\sigma_t$  is increasing, we have

$$\int_0^{t_{\text{SSI}}} \dot{\sigma}_t dt = \sigma_{t_{\text{SSI}}} - \sigma_0 = \sigma_{t_{\text{SSI}}}.$$

Taking absolute value and noting that  $\sigma_0 = 0$ ,

$$\left\| \int_{t_{\text{SSI}}}^0 -\dot{\sigma}_t \sigma_t \nabla_{\mathbf{x}} \log p(\hat{\mathbf{x}}_t; \sigma_t) dt \right\|_2 \leq C \sigma_{t_{\text{SSI}}}.$$

For the second term,  $\|\sigma_{t_{\text{SSI}}} \mathbf{n}\|_2 = \sigma_{t_{\text{SSI}}} \|\mathbf{n}\|_2$  where  $\mathbf{n} \sim \mathcal{N}(\mathbf{0}, \mathbf{I})$ . The squared  $L^2$  norm  $\|\mathbf{n}\|_2^2$  follows a  $\chi^2$ -distribution with  $d$  degrees of freedom. By the tail bound from [Laurent & Massart \(2000\)](#), for any  $\delta \in (0, 1)$ , with probability at least  $1 - \delta$ ,

$$\|\mathbf{n}\|_2^2 \leq d + 2\sqrt{-d \log \delta} - 2 \log \delta,$$

which implies

$$\|\mathbf{n}\|_2 \leq \sqrt{d + 2\sqrt{-d \log \delta} - 2 \log \delta}.$$

Therefore, combining both terms via the triangle inequality, with probability at least  $1 - \delta$ ,

$$\|\mathbf{x}_0 - \hat{\mathbf{x}}_0\|_2 \leq C \sigma_{t_{\text{SSI}}} + \sigma_{t_{\text{SSI}}} \sqrt{d + 2\sqrt{-d \log \delta} - 2 \log \delta} = \sigma_{t_{\text{SSI}}} \left( C + \sqrt{d + 2\sqrt{-d \log \delta} - 2 \log \delta} \right),$$

completing the proof.  $\square$

### A.2. Singularity Analysis of Score Functions

In this section, we provide a detailed theoretical analysis of the singular behavior of score functions in diffusion models. Following the work of [Lu et al. \(2023\)](#), for the VE process defined by  $p(\mathbf{x}; \sigma)$ , we establish the following results.

We denote by  $\Omega \subset \mathbb{R}^d$  an  $n$ -dimensional smooth sub-manifold with  $n < d$ . To characterize the asymptotic behavior of score functions for general data distributions supported on such manifolds, we introduce the following geometric assumptions on the sampling trajectory points  $\mathbf{x}_t$  and the data distribution  $p_{\text{data}}$ .

**Assumption 1** (Unique projection). For a given fixed point  $\mathbf{x} \in \mathbb{R}^d \setminus \Omega$ , there exists a unique point  $\mathbf{y}_x \in \Omega$  that minimizes the distance to  $\mathbf{x}$ , i.e.,

$$\mathbf{y}_x = \operatorname{argmin}_{\mathbf{y} \in \Omega} \|\mathbf{x} - \mathbf{y}\|.$$

**Assumption 2** (Local low-dimensional structure). Let  $B_\varepsilon = \{\mathbf{y} \in \Omega : \|\mathbf{y} - \mathbf{x}\| < \|\mathbf{y}_x - \mathbf{x}\| + \varepsilon\}$ , which is a decreasing family of sets as  $\varepsilon \rightarrow 0$ . There exists  $\varepsilon_0 > 0$  such that for  $\mathbf{y} \in B_{\varepsilon_0}$ , there exists a local coordinate chart  $\mathbf{z} \mapsto \mathbf{y}(\mathbf{z}) \in B_{\varepsilon_0} \subset \Omega$ , under which the data distribution admits a smooth density in the form

$$p_{\text{data}}(\mathbf{y}) = \hat{\rho}(\mathbf{z})|J(\mathbf{z})|\delta_{\mathbf{y}(\mathbf{z}) \in \Omega},$$

where  $J(\mathbf{z})$  is the Jacobian of the coordinate transformation, corresponding to the dimension  $n$  of the local variable  $\mathbf{z}$ . Moreover, within  $\mathbf{y}(\mathbf{z}) \in B_{\varepsilon_0}$ , the density is bounded away from zero and infinity:

$$0 < \rho_0 \leq \hat{\rho}(\mathbf{z})|J(\mathbf{z})| \leq \rho_1 < \infty.$$

We first establish the main result on the singularity of the score function, which characterizes its explosive behavior near  $t = 0$ .

**Theorem 3** (Singularity of score function in VE SDE). *Fix  $\mathbf{x} \notin \Omega$  and let the data distribution  $p_{\text{data}}$  satisfy Assumptions 1 and 2. Then the score function  $\nabla_{\mathbf{x}} \log p(\mathbf{x}; \sigma_t)$  blows up as  $\sigma_t \rightarrow 0$ , and more precisely, satisfies*

$$\nabla_{\mathbf{x}} \log p(\mathbf{x}; \sigma_t) = \frac{\mathbf{x} - \mathbf{y}_x}{\sigma_t^2} (1 + o(1)), \quad \text{as } \sigma_t \rightarrow 0,$$

where  $\mathbf{y}_x = \operatorname{argmin}_{\mathbf{x}_0 \in \Omega} \|\mathbf{x} - \mathbf{x}_0\|$ .

### Proof of Theorem 3

The proof follows the approach of [Lu et al. \(2023\)](#), who use Laplace's method to establish pointwise convergence singularity. We extend their analysis to the VE framework.

For a fixed  $\mathbf{x} \notin \Omega$ , the score function has the following representation:

$$\nabla_{\mathbf{x}} \log p(\mathbf{x}; \sigma_t) = \frac{\mathbb{E}[\mathbf{x}_0 | \mathbf{x}] - \mathbf{x}}{\sigma_t^2} = \frac{g(\mathbf{x}, t)}{\sigma_t^2},$$

where

$$g(\mathbf{x}, t) = \mathbb{E}[\mathbf{x}_0 | \mathbf{x}] - \mathbf{x} = \frac{\int_{\Omega} (\mathbf{y} - \mathbf{x}) \exp\left(-\frac{\|\mathbf{x} - \mathbf{y}\|^2}{2\sigma_t^2}\right) p_{\text{data}}(\mathbf{y}) d\mathbf{y}}{\int_{\Omega} \exp\left(-\frac{\|\mathbf{x} - \mathbf{y}\|^2}{2\sigma_t^2}\right) p_{\text{data}}(\mathbf{y}) d\mathbf{y}}.$$

By Assumption 1, there exists a unique projection point  $\mathbf{y}_x \in \Omega$  that minimizes the distance to  $\mathbf{x}$ . Let  $r = \|\mathbf{x} - \mathbf{y}_x\|$  denote the distance from  $\mathbf{x}$  to the manifold. With a fixed  $\varepsilon > 0$ , we decompose  $g$  into two parts:

$$g(\mathbf{x}, t) = \frac{\int_{B_\varepsilon} (\mathbf{y} - \mathbf{x}) \exp\left(-\frac{\|\mathbf{x} - \mathbf{y}\|^2}{2\sigma_t^2}\right) p_{\text{data}}(\mathbf{y}) d\mathbf{y}}{\int_{\Omega} \exp\left(-\frac{\|\mathbf{x} - \mathbf{y}\|^2}{2\sigma_t^2}\right) p_{\text{data}}(\mathbf{y}) d\mathbf{y}} + \frac{\int_{\Omega \setminus B_\varepsilon} (\mathbf{y} - \mathbf{x}) \exp\left(-\frac{\|\mathbf{x} - \mathbf{y}\|^2}{2\sigma_t^2}\right) p_{\text{data}}(\mathbf{y}) d\mathbf{y}}{\int_{\Omega} \exp\left(-\frac{\|\mathbf{x} - \mathbf{y}\|^2}{2\sigma_t^2}\right) p_{\text{data}}(\mathbf{y}) d\mathbf{y}},$$

where

$$B_\varepsilon = \{\mathbf{y} \in \Omega : \|\mathbf{y} - \mathbf{x}\| < r + \varepsilon\},$$

as in Assumption 2.

By definition of  $B_\varepsilon$ , for  $\mathbf{y} \in \Omega \setminus B_\varepsilon$ , we have

$$\|\mathbf{x} - \mathbf{y}\| \geq r + \varepsilon = \|\mathbf{x} - \mathbf{y}_x\| + \varepsilon.$$

For  $\mathbf{y} \in B_\varepsilon$ , we have

$$\|\mathbf{x} - \mathbf{y}\| \leq r + \varepsilon = \|\mathbf{x} - \mathbf{y}_x\| + \varepsilon.$$

We claim that the second term of the decomposition converges to zero as  $\sigma_t \rightarrow 0$  (with fixed  $\varepsilon$ ) since

$$\begin{aligned} \left\| \frac{\int_{\Omega \setminus B_\varepsilon} (\mathbf{y} - \mathbf{x}) \exp\left(-\frac{\|\mathbf{x} - \mathbf{y}\|^2}{2\sigma_t^2}\right) p_{\text{data}}(\mathbf{y}) d\mathbf{y}}{\int_{\Omega} \exp\left(-\frac{\|\mathbf{x} - \mathbf{y}\|^2}{2\sigma_t^2}\right) p_{\text{data}}(\mathbf{y}) d\mathbf{y}} \right\| &\leq \frac{\int_{\Omega \setminus B_\varepsilon} (\|\mathbf{x}\| + \|\mathbf{y}\|) \exp\left(-\frac{(r + \varepsilon)^2}{2\sigma_t^2}\right) p_{\text{data}}(\mathbf{y}) d\mathbf{y}}{\int_{\Omega} \exp\left(-\frac{\|\mathbf{x} - \mathbf{y}\|^2}{2\sigma_t^2}\right) p_{\text{data}}(\mathbf{y}) d\mathbf{y}} \\ &\leq \frac{\int_{\Omega \setminus B_\varepsilon} (\|\mathbf{x}\| + \|\mathbf{y}\|) p_{\text{data}}(\mathbf{y}) d\mathbf{y}}{\int_{\Omega} \exp\left(-\frac{\|\mathbf{x} - \mathbf{y}\|^2 - (r + \varepsilon)^2}{2\sigma_t^2}\right) p_{\text{data}}(\mathbf{y}) d\mathbf{y}}. \end{aligned}$$

Given the boundedness of the expectation of the data distribution  $p_{\text{data}}$ , it remains to show the denominator converges to infinity as  $\sigma_t \rightarrow 0$ . In fact, with the Subspace Assumption 2 in mind, consider a slightly smaller set:

$$B_{\varepsilon'} = \{\mathbf{y} \in \Omega : \|\mathbf{y} - \mathbf{x}\| < r + \varepsilon'\},$$

where  $\varepsilon' = \varepsilon/2$ . Clearly  $B_{\varepsilon'} \subset B_\varepsilon$ .

Then

$$\begin{aligned} \int_{\Omega} \exp\left(-\frac{\|\mathbf{x} - \mathbf{y}\|^2 - (r + \varepsilon)^2}{2\sigma_t^2}\right) p_{\text{data}}(\mathbf{y}) d\mathbf{y} &\geq \int_{B_{\varepsilon'}} \exp\left(-\frac{\|\mathbf{x} - \mathbf{y}\|^2 - (r + \varepsilon)^2}{2\sigma_t^2}\right) p_{\text{data}}(\mathbf{y}) d\mathbf{y} \\ &\geq \int_{\mathbf{y}(\mathbf{z}) \in B_{\varepsilon'}} \exp\left(-\frac{(r + \varepsilon')^2 - (r + \varepsilon)^2}{2\sigma_t^2}\right) \hat{\rho}(\mathbf{z}) |J(\mathbf{z})| d\mathbf{z}, \end{aligned}$$

where we have used the fact that for  $\mathbf{y} \in B_{\varepsilon'}$ , we have  $\|\mathbf{x} - \mathbf{y}\| \leq r + \varepsilon'$ .

Compute the exponent:

$$\begin{aligned} (r + \varepsilon')^2 - (r + \varepsilon)^2 &= r^2 + 2r\varepsilon' + \varepsilon'^2 - (r^2 + 2r\varepsilon + \varepsilon^2) \\ &= 2r(\varepsilon' - \varepsilon) + (\varepsilon'^2 - \varepsilon^2) \\ &= 2r \cdot \left(-\frac{\varepsilon}{2}\right) + \left(\frac{\varepsilon^2}{4} - \varepsilon^2\right) \\ &= -r\varepsilon - \frac{3}{4}\varepsilon^2. \end{aligned}$$

Since  $\varepsilon > 0$  is fixed and  $r > 0$ , we have

$$\frac{(r + \varepsilon')^2 - (r + \varepsilon)^2}{\sigma_t^2} = \frac{-r\varepsilon - \frac{3}{4}\varepsilon^2}{\sigma_t^2} \rightarrow -\infty, \quad \text{as } \sigma_t \rightarrow 0,$$

which implies the denominator converges to infinity. Similarly, since for  $\mathbf{y} \in B_{\varepsilon'}$  we have  $\|\mathbf{x} - \mathbf{y}\| \leq r + \varepsilon'$ , while for  $\mathbf{y} \in \Omega \setminus B_\varepsilon$  we have  $\|\mathbf{x} - \mathbf{y}\| \geq r + \varepsilon$ , the ratio

$$\frac{\int_{\Omega \setminus B_\varepsilon} \exp\left(-\frac{\|\mathbf{x} - \mathbf{y}\|^2}{2\sigma_t^2}\right) p_{\text{data}}(\mathbf{y}) d\mathbf{y}}{\int_{B_\varepsilon} \exp\left(-\frac{\|\mathbf{x} - \mathbf{y}\|^2}{2\sigma_t^2}\right) p_{\text{data}}(\mathbf{y}) d\mathbf{y}} \leq C_\varepsilon \exp\left(-\frac{(r + \varepsilon)^2 - (r + \varepsilon')^2}{2\sigma_t^2}\right) = o(t),$$

as  $\sigma_t \rightarrow 0$ , where the last equality follows from the fact that the exponent tends to  $-\infty$  as shown above.

So the denominator in the first term can also be decomposed and approximated by the contribution in  $B_\varepsilon$ :

$$\int_{\Omega} \exp\left(-\frac{\|\mathbf{x} - \mathbf{y}\|^2}{2\sigma_t^2}\right) p_{\text{data}}(\mathbf{y}) d\mathbf{y} = (1 + o(t)) \int_{B_\varepsilon} \exp\left(-\frac{\|\mathbf{x} - \mathbf{y}\|^2}{2\sigma_t^2}\right) p_{\text{data}}(\mathbf{y}) d\mathbf{y},$$

as  $\sigma_t \rightarrow 0$ .

Then when  $\sigma_t \rightarrow 0$ , we have in local coordinates (2),

$$\begin{aligned} \frac{\int_{B_\varepsilon} (\mathbf{y} - \mathbf{x}) \exp\left(-\frac{\|\mathbf{x} - \mathbf{y}\|^2}{2\sigma_t^2}\right) p_{\text{data}}(\mathbf{y}) d\mathbf{y}}{\int_{B_\varepsilon} \exp\left(-\frac{\|\mathbf{x} - \mathbf{y}\|^2}{2\sigma_t^2}\right) p_{\text{data}}(\mathbf{y}) d\mathbf{y}} &= \frac{\int_{\mathbf{y}(\mathbf{z}) \in B_\varepsilon} (\mathbf{y}(\mathbf{z}) - \mathbf{x}) \exp\left(-\frac{\|\mathbf{x} - \mathbf{y}(\mathbf{z})\|^2}{2\sigma_t^2}\right) \hat{\rho}(\mathbf{z}) |J(\mathbf{z})| d\mathbf{z}}{\int_{\mathbf{y}(\mathbf{z}) \in B_\varepsilon} \exp\left(-\frac{\|\mathbf{x} - \mathbf{y}(\mathbf{z})\|^2}{2\sigma_t^2}\right) \hat{\rho}(\mathbf{z}) |J(\mathbf{z})| d\mathbf{z}} \\ &= \mathbf{x} - \frac{\int_{\mathbf{y}(\mathbf{z}) \in B_\varepsilon} \mathbf{y}(\mathbf{z}) \exp\left(-\frac{\|\mathbf{x} - \mathbf{y}(\mathbf{z})\|^2}{2\sigma_t^2}\right) \hat{\rho}(\mathbf{z}) |J(\mathbf{z})| d\mathbf{z}}{\int_{\mathbf{y}(\mathbf{z}) \in B_\varepsilon} \exp\left(-\frac{\|\mathbf{x} - \mathbf{y}(\mathbf{z})\|^2}{2\sigma_t^2}\right) \hat{\rho}(\mathbf{z}) |J(\mathbf{z})| d\mathbf{z}}. \end{aligned}$$

Taking (2) into account, that  $\mathbf{y}(\mathbf{z})$  is well approximated by  $\mathbf{y}_x$  on  $B_\varepsilon$  for  $\sigma_t$  small, we claim that

$$\sup_{\mathbf{y} \in B_\varepsilon} \|\mathbf{y} - \mathbf{y}_x\| \rightarrow 0, \quad \text{as } \varepsilon \rightarrow 0.$$

To see this, suppose the claim does not hold. Then there exists a sequence  $\{\mathbf{y}_i\} \subset \Omega$  such that  $\lim_{i \rightarrow \infty} \|\mathbf{x} - \mathbf{y}_i\| = r$ , and there exists  $\eta > 0$  such that  $\|\mathbf{y}_i - \mathbf{y}_x\| \geq \eta$  for all  $i$ . Since  $\Omega$  is closed, the sequence  $\{\mathbf{y}_i\}$  admits a convergent subsequence with limit  $\mathbf{y}^* \in \Omega$ . By continuity, we have  $\|\mathbf{x} - \mathbf{y}^*\| = r$  and  $\|\mathbf{y}^* - \mathbf{y}_x\| \geq \eta > 0$ , which contradicts Assumption 1 that  $\mathbf{y}_x$  is the unique point minimizing the distance to  $\mathbf{x}$ .

With this result, it follows that

$$\begin{aligned} &\left\| \frac{\int_{\mathbf{y}(\mathbf{z}) \in B_\varepsilon} \mathbf{y}(\mathbf{z}) \exp\left(-\frac{\|\mathbf{x} - \mathbf{y}(\mathbf{z})\|^2}{2\sigma_t^2}\right) \hat{\rho}(\mathbf{z}) |J(\mathbf{z})| d\mathbf{z}}{\int_{\mathbf{y}(\mathbf{z}) \in B_\varepsilon} \exp\left(-\frac{\|\mathbf{x} - \mathbf{y}(\mathbf{z})\|^2}{2\sigma_t^2}\right) \hat{\rho}(\mathbf{z}) |J(\mathbf{z})| d\mathbf{z}} - \mathbf{y}_x \right\| \\ &\leq \frac{\rho_1 \int_{\mathbf{y}(\mathbf{z}) \in B_\varepsilon} \|\mathbf{y}(\mathbf{z}) - \mathbf{y}_x\| \exp\left(-\frac{\|\mathbf{x} - \mathbf{y}(\mathbf{z})\|^2}{2\sigma_t^2}\right) d\mathbf{z}}{\rho_0 \int_{\mathbf{y}(\mathbf{z}) \in B_\varepsilon} \exp\left(-\frac{\|\mathbf{x} - \mathbf{y}(\mathbf{z})\|^2}{2\sigma_t^2}\right) d\mathbf{z}} \\ &\leq \frac{\rho_1}{\rho_0} \sup_{\mathbf{y} \in B_\varepsilon} \|\mathbf{y} - \mathbf{y}_x\|, \end{aligned}$$

which can be made arbitrarily small by choosing  $\varepsilon$  sufficiently small.

Substituting back to the decomposition of  $g(\mathbf{x}, t)$ , we have

$$\lim_{t \rightarrow 0} g(\mathbf{x}, t) = \mathbf{x} - \mathbf{y}_x + O(\varepsilon).$$

Since the choice of  $\varepsilon > 0$  is arbitrary, from the representation of the score function we have:

$$\lim_{t \rightarrow 0} \sigma_t^2 \nabla_{\mathbf{x}} \log p(\mathbf{x}; \sigma_t) = \lim_{t \rightarrow 0} g(\mathbf{x}, t) = \mathbf{x} - \mathbf{y}_x,$$

which implies

$$\nabla_{\mathbf{x}} \log p(\mathbf{x}; \sigma_t) = \frac{\mathbf{x} - \mathbf{y}_x}{\sigma_t^2} (1 + o(1)) \quad \text{as } \sigma_t \rightarrow 0,$$

which establishes the desired singularity result.

*Remark 4.* Theorem 3 establishes that, in the pointwise sense, the conditional expectation  $\mathbb{E}[\mathbf{x}_0|\mathbf{x}]$  in its convolution representation contracts to the projection point  $\mathbf{y}_\mathbf{x}$  of  $\mathbf{x}$  onto the manifold  $\Omega$ . More precisely, the difference  $\mathbb{E}[\mathbf{x}_0|\mathbf{x}] - \mathbf{x}$  is dominated by the projection vector  $\mathbf{y}_\mathbf{x} - \mathbf{x}$ , which gives rise to the singularity of the score function of the form  $\nabla_{\mathbf{x}} \log p(\mathbf{x}; \sigma_t) = \frac{(\mathbf{x} - \mathbf{y}_\mathbf{x})}{\sigma_t^2} (1 + o(1))$  as  $\sigma_t \rightarrow 0$ .

### A.3. Projection distance along sampling trajectory

To further characterize the behavior along sampling trajectories, we establish a concentration result that quantifies the distance between noisy variables and their projections onto the data manifold.

**Theorem 5** (Concentration of the projected distance). *Let  $\Omega \subset \mathbb{R}^d$  be a  $C^2$  embedded submanifold of dimension  $n < d$ , and fix  $\mathbf{x}_0 \in \Omega$ . Consider the forward diffusion process*

$$\mathbf{x}_t = \mathbf{x}_0 + \sigma_t \mathbf{n}, \quad \mathbf{n} \sim \mathcal{N}(\mathbf{0}, \mathbf{I}_d),$$

where  $\sigma_t = \sigma(t) > 0$  is a differentiable noise schedule with  $\sigma_t \rightarrow 0$  as  $t \rightarrow 0$ . For sufficiently small  $t$ , let  $\mathbf{y}_{\mathbf{x}_t} \in \Omega$  be the unique projection of  $\mathbf{x}_t$  onto  $\Omega$ . Then, for any  $\varepsilon > 0$  there exist constants  $c_\varepsilon, C_\varepsilon > 0$  (depending only on  $d, n$ , and  $\varepsilon$ ) and  $t_0 > 0$  such that for all  $0 < t < t_0$ ,

$$\mathbb{P}\left(c_\varepsilon \sigma_t \leq \|\mathbf{x}_t - \mathbf{y}_{\mathbf{x}_t}\| \leq C_\varepsilon \sigma_t\right) \geq 1 - \varepsilon.$$

### Proof of Theorem 5

*Proof.* Let  $\mathbf{y} : U \rightarrow \Omega$  be a local  $C^2$  parametrization of  $\Omega$  around  $\mathbf{x}_0$  with  $\mathbf{y}(\mathbf{0}) = \mathbf{x}_0$ , where  $U \subset \mathbb{R}^n$  is an open neighborhood of  $\mathbf{0}$ . Let  $J = D\mathbf{y}(\mathbf{0}) \in \mathbb{R}^{d \times n}$  be the Jacobian matrix of  $\mathbf{y}$  at  $\mathbf{0}$ . The columns of  $J$  are linearly independent and span the tangent space  $T_{\mathbf{x}_0} \Omega = \text{Im}(J)$ . Let  $N_{\mathbf{x}_0} \Omega = (\text{Im}(J))^\perp$  be the normal space.

Decompose the Gaussian noise  $\mathbf{n}$  into its tangential and normal components:

$$\mathbf{n} = \mathbf{n}_\parallel + \mathbf{n}_\perp, \quad \mathbf{n}_\parallel \in \text{Im}(J), \quad \mathbf{n}_\perp \in N_{\mathbf{x}_0} \Omega.$$

Since  $\text{Im}(J)$  and  $N_{\mathbf{x}_0} \Omega$  are orthogonal subspaces,  $\mathbf{n}_\parallel$  and  $\mathbf{n}_\perp$  are independent Gaussian vectors with  $\mathbf{n}_\perp \sim \mathcal{N}(\mathbf{0}, \mathbf{I}_{d-n})$  (in suitable coordinates).

We first establish an upper bound. Because  $\mathbf{n}_\parallel \in \text{Im}(J)$ , there exists a vector  $\mathbf{z} \in \mathbb{R}^n$  such that  $J\mathbf{z} = \sigma_t \mathbf{n}_\parallel$ . For sufficiently small  $\sigma_t$ ,  $\mathbf{z}$  lies in  $U$  and we can define  $\tilde{\mathbf{y}} = \mathbf{y}(\mathbf{z})$ . By the  $C^2$  property, we have the expansion

$$\tilde{\mathbf{y}} = \mathbf{x}_0 + J\mathbf{z} + R(\mathbf{z}), \quad \|R(\mathbf{z})\| = O(\|\mathbf{z}\|^2).$$

Since  $\|\mathbf{z}\| = O(\sigma_t)$  (because  $J$  is injective and  $\sigma_t \mathbf{n}_\parallel$  is of order  $\sigma_t$ ), we have  $\|R(\mathbf{z})\| = O(\sigma_t^2)$ . Now,

$$\begin{aligned} \|\mathbf{x}_t - \tilde{\mathbf{y}}\| &= \|\mathbf{x}_0 + \sigma_t \mathbf{n} - (\mathbf{x}_0 + J\mathbf{z} + R(\mathbf{z}))\| \\ &= \|\sigma_t \mathbf{n}_\parallel + \sigma_t \mathbf{n}_\perp - J\mathbf{z} - R(\mathbf{z})\| \\ &= \|\sigma_t \mathbf{n}_\perp - R(\mathbf{z})\| \leq \sigma_t \|\mathbf{n}_\perp\| + \|R(\mathbf{z})\|. \end{aligned}$$

Because  $\mathbf{y}_{\mathbf{x}_t}$  is the projection of  $\mathbf{x}_t$  onto  $\Omega$ , we have  $\|\mathbf{x}_t - \mathbf{y}_{\mathbf{x}_t}\| \leq \|\mathbf{x}_t - \tilde{\mathbf{y}}\|$ , hence

$$\|\mathbf{x}_t - \mathbf{y}_{\mathbf{x}_t}\| \leq \sigma_t \|\mathbf{n}_\perp\| + O(\sigma_t^2).$$

For the lower bound, we first note that from the upper bound and the fact that  $\|\mathbf{x}_t - \mathbf{x}_0\| = \sigma_t \|\mathbf{n}\|$ , we have

$$\|\mathbf{y}_{\mathbf{x}_t} - \mathbf{x}_0\| \leq \|\mathbf{y}_{\mathbf{x}_t} - \mathbf{x}_t\| + \|\mathbf{x}_t - \mathbf{x}_0\| \leq \sigma_t \|\mathbf{n}_\perp\| + O(\sigma_t^2) + \sigma_t \|\mathbf{n}\| \leq 2\sigma_t \|\mathbf{n}\| + O(\sigma_t^2).$$

Since  $\|\mathbf{n}\|$  is almost surely bounded, when  $\sigma_t$  is sufficiently small, the projection point  $\mathbf{y}_{\mathbf{x}_t}$  converges to  $\mathbf{x}_0$ . Therefore, we can apply the local expansion at  $\mathbf{x}_0$ : write  $\mathbf{y}_{\mathbf{x}_t} = \mathbf{y}(\mathbf{z}_t)$  for some  $\mathbf{z}_t \in U$  with  $\mathbf{z}_t \rightarrow \mathbf{0}$ . Then

$$\mathbf{y}_{\mathbf{x}_t} = \mathbf{x}_0 + J\mathbf{z}_t + R(\mathbf{z}_t), \quad \|R(\mathbf{z}_t)\| = O(\|\mathbf{z}_t\|^2).$$

Now consider the squared distance:

$$\begin{aligned}\|\mathbf{x}_t - \mathbf{y}_{\mathbf{x}_t}\|^2 &= \|\sigma_t \mathbf{n} - J\mathbf{z}_t - R(\mathbf{z}_t)\|^2 \\ &= \|\sigma_t \mathbf{n}_{\parallel} - J\mathbf{z}_t + \sigma_t \mathbf{n}_{\perp} - R(\mathbf{z}_t)\|^2.\end{aligned}$$

Because the subspaces  $\text{Im}(J)$  and  $N_{\mathbf{x}_0}\Omega$  are orthogonal, we can decompose the squared norm into two orthogonal components:

$$\|\mathbf{x}_t - \mathbf{y}_{\mathbf{x}_t}\|^2 = \|\sigma_t \mathbf{n}_{\parallel} - J\mathbf{z}_t - R_{\parallel}(\mathbf{z}_t)\|^2 + \|\sigma_t \mathbf{n}_{\perp} - R_{\perp}(\mathbf{z}_t)\|^2,$$

where  $R_{\perp}(\mathbf{z}_t)$  denotes the projection of  $R(\mathbf{z}_t)$  onto  $N_{\mathbf{x}_0}\Omega$  (the tangential component of  $R(\mathbf{z}_t)$  is absorbed into the first term). Since  $\|\sigma_t \mathbf{n}_{\parallel} - J\mathbf{z}_t\|^2 \geq 0$ , we obtain

$$\|\mathbf{x}_t - \mathbf{y}_{\mathbf{x}_t}\|^2 \geq \|\sigma_t \mathbf{n}_{\perp} - R_{\perp}(\mathbf{z}_t)\|^2.$$

Now,

$$\|\sigma_t \mathbf{n}_{\perp} - R_{\perp}(\mathbf{z}_t)\| \geq \sigma_t \|\mathbf{n}_{\perp}\| - \|R_{\perp}(\mathbf{z}_t)\| \geq \sigma_t \|\mathbf{n}_{\perp}\| - \|R(\mathbf{z}_t)\|.$$

Thus

$$\|\mathbf{x}_t - \mathbf{y}_{\mathbf{x}_t}\| \geq \sigma_t \|\mathbf{n}_{\perp}\| - \|R(\mathbf{z}_t)\|.$$

It remains to bound  $\|\mathbf{z}_t\|$  and hence  $\|R(\mathbf{z}_t)\|$ . From the bound  $\|\mathbf{y}_{\mathbf{x}_t} - \mathbf{x}_0\| \leq 2\sigma_t \|\mathbf{n}\| + O(\sigma_t^2)$ , we have  $\|\mathbf{y}_{\mathbf{x}_t} - \mathbf{x}_0\| = O(\sigma_t)$ . Because  $J$  is injective, there exists a constant  $c > 0$  such that  $\|J\mathbf{z}_t\| \geq c\|\mathbf{z}_t\|$  for all  $\mathbf{z}_t$  (this follows from the compactness of the unit sphere in  $\mathbb{R}^n$ ). Moreover,  $\|R(\mathbf{z}_t)\| = O(\|\mathbf{z}_t\|^2)$ . Therefore,

$$\|\mathbf{y}_{\mathbf{x}_t} - \mathbf{x}_0\| = \|J\mathbf{z}_t + R(\mathbf{z}_t)\| \geq \|J\mathbf{z}_t\| - \|R(\mathbf{z}_t)\| \geq c\|\mathbf{z}_t\| - O(\|\mathbf{z}_t\|^2),$$

which implies  $\|\mathbf{z}_t\| = O(\sigma_t)$ . Consequently,  $\|R(\mathbf{z}_t)\| = O(\sigma_t^2)$ .

Combining the upper and lower bounds yields

$$\sigma_t \|\mathbf{n}_{\perp}\| - O(\sigma_t^2) \leq \|\mathbf{x}_t - \mathbf{y}_{\mathbf{x}_t}\| \leq \sigma_t \|\mathbf{n}_{\perp}\| + O(\sigma_t^2),$$

for all sufficiently small  $t$ . Moreover, based on the above derivation, the projection distance is dominated by the norm of the normal component  $\|\mathbf{n}_{\perp}\|$  of the random noise as  $t \rightarrow 0$ .

Now,  $\|\mathbf{n}_{\perp}\|$  is the norm of a Gaussian vector of dimension  $d - n$ . Following Theorem 3.1.1 of Vershynin (2018), we have for any  $A > 0$ ,

$$\mathbb{P}(|\|\mathbf{n}_{\perp}\| - \sqrt{d-n}| > A) \leq 2 \exp(-kA^2),$$

where  $k > 0$  is an absolute constant. Choose  $u_{\varepsilon}$  large enough so that  $2 \exp(-kA_{\varepsilon}^2) \leq \varepsilon$ . Then with probability at least  $1 - \varepsilon$ ,

$$\sqrt{d-n} - A_{\varepsilon} \leq \|\mathbf{n}_{\perp}\| \leq \sqrt{d-n} + A_{\varepsilon}.$$

For sufficiently small  $t$ , the  $O(\sigma_t^2)$  terms are dominated by  $\sigma_t A_{\varepsilon}$ . Consequently, with probability at least  $1 - \varepsilon$ ,

$$\begin{aligned}\|\mathbf{x}_t - \mathbf{y}_{\mathbf{x}_t}\| &\leq \sigma_t (\sqrt{d-n} + A_{\varepsilon}) + O(\sigma_t^2) \leq \sigma_t (\sqrt{d-n} + 2A_{\varepsilon}), \\ \|\mathbf{x}_t - \mathbf{y}_{\mathbf{x}_t}\| &\geq \sigma_t (\sqrt{d-n} - A_{\varepsilon}) - O(\sigma_t^2) \geq \sigma_t (\sqrt{d-n} - 2A_{\varepsilon}).\end{aligned}$$

Setting  $c_{\varepsilon} = \sqrt{d-n} - 2A_{\varepsilon}$  and  $C_{\varepsilon} = \sqrt{d-n} + 2A_{\varepsilon}$  completes the proof.  $\square$

*Remark 6.* Theorem 5 reveals a fundamental geometric property of diffusion models when applied to data distributions supported on low-dimensional manifolds. Since manifolds are measure-zero sets in the ambient space, noisy variables  $\mathbf{x}_t$  generated by the forward diffusion process almost surely lie outside the manifold. Due to concentration properties of Gaussian norms, the projection distance  $\|\mathbf{x}_t - \mathbf{y}_{\mathbf{x}_t}\|$  is tightly concentrated around  $\sigma_t$  with high probability, providing a quantitative characterization of the leading-order term in the score function singularity.

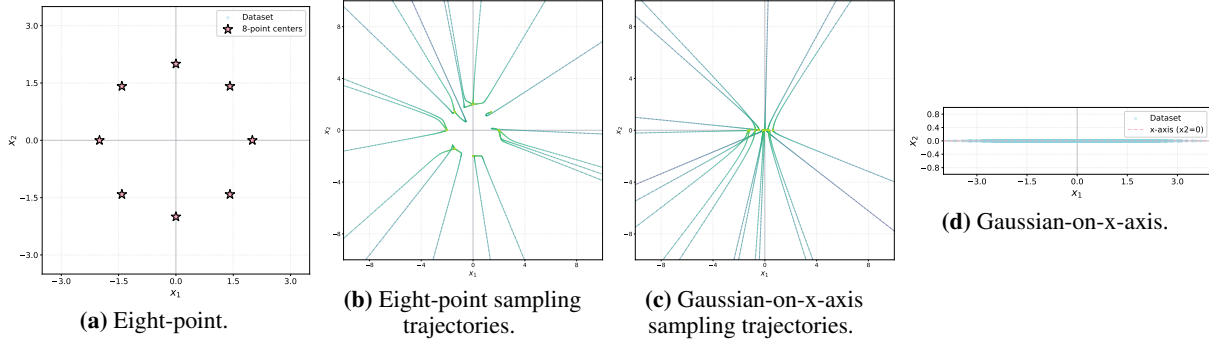


Figure 13. Data distribution visualizations for the two low-dimensional manifold distributions used in our validation experiments.

#### A.4. Validation Experiments on Low-Dimensional Manifold Distributions

To empirically validate the theoretical results established in Theorems 3 and 5, we conduct comprehensive experiments on two canonical low-dimensional manifold distributions where the score functions can be computed exactly. We consider two representative distributions in  $\mathbb{R}^2$ :

**1. Eight-Point Distribution:** The data distribution consists of eight discrete points uniformly distributed on a circle of radius  $R = 2$ :

$$p_{\text{data}}(\mathbf{x}) = \frac{1}{8} \sum_{k=1}^8 \delta(\mathbf{x} - \boldsymbol{\mu}_k),$$

where  $\boldsymbol{\mu}_k = (2 \cos \theta_k, 2 \sin \theta_k)$  with  $\theta_k \in \{\pi, 3\pi/4, \pi/2, \pi/4, 0, -\pi/4, -\pi/2, -3\pi/4\}$ . The noisy distribution  $p(\mathbf{x}; \sigma)$  is a Gaussian mixture:

$$p(\mathbf{x}; \sigma) = \frac{1}{8} \sum_{k=1}^8 \mathcal{N}(\mathbf{x} | \boldsymbol{\mu}_k, \sigma^2 \mathbf{I}),$$

and the exact score function takes the form:

$$\nabla_{\mathbf{x}} \log p(\mathbf{x}; \sigma) = \sum_{k=1}^8 \omega_k(\mathbf{x}) \frac{\boldsymbol{\mu}_k - \mathbf{x}}{\sigma^2},$$

where  $\omega_k(\mathbf{x}) = \frac{\exp(-\|\mathbf{x} - \boldsymbol{\mu}_k\|^2/(2\sigma^2))}{\sum_{j=1}^8 \exp(-\|\mathbf{x} - \boldsymbol{\mu}_j\|^2/(2\sigma^2))}$  are the normalized posterior responsibilities (softmax probabilities).

**2. Gaussian-on-x-axis Distribution:** The data distribution is a standard Gaussian along the  $x_1$ -axis with  $x_2 = 0$ :

$$p_{\text{data}}(\mathbf{x}) = \mathcal{N}(x_1 | 0, 1) \cdot \delta(x_2),$$

where  $\delta(\cdot)$  denotes the Dirac delta function. The noisy distribution  $p(\mathbf{x}; \sigma)$  is:

$$p(\mathbf{x}; \sigma) = \mathcal{N}(x_1 | 0, \sigma^2 + 1) \cdot \mathcal{N}(x_2 | 0, \sigma^2),$$

and the exact score function is:

$$\nabla_{\mathbf{x}} \log p(\mathbf{x}; \sigma) = \left( -\frac{x_1}{\sigma^2 + 1}, -\frac{x_2}{\sigma^2} \right)^T.$$

For both distributions, we perform VE (Variance Exploding) process sampling using the exact score functions with the EDM framework (Karras et al., 2022). We use the Karras noise schedule with  $\sigma_{\min} = 0.002$ ,  $\sigma_{\max} = 80.0$ ,  $\rho = 7.0$ , and 200 sampling steps, employing the Heun method for numerical integration of the probability flow ODE. We generate 200,000 samples for each distribution and visualize both the data distributions and the sampling trajectories. The distribution visualizations (Fig. 13) clearly show the low-dimensional manifold structure: the eight-point distribution concentrates on eight discrete points, while the Gaussian-on-x-axis distribution concentrates along the  $x_1$ -axis.

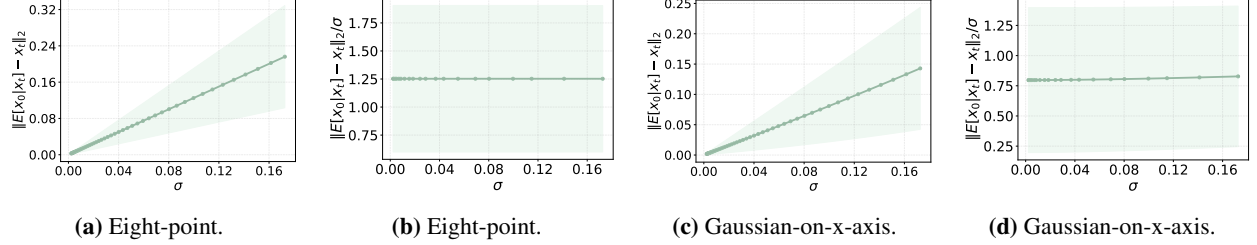


Figure 14. Normalized projection distance  $\|\mathbb{E}[\mathbf{x}_0|\mathbf{x}_t] - \mathbf{x}_t\|_2 / \sigma_t$  along sampling trajectories. The boundedness and convergence to a constant as  $\sigma_t \rightarrow 0$  provides quantitative validation of Theorem 5.

The sampling trajectory visualizations (Fig. 13) demonstrate the reverse diffusion process, where samples evolve from high-noise regions (initialized at  $\sigma_{\max} = 80$ ) toward the data manifold. The trajectories exhibit smooth convergence paths, with points gradually moving toward their respective manifold structures as the noise level  $\sigma_t$  decreases.

To quantitatively validate the singularity behavior of score function, we analyze the evolution of  $\|\mathbb{E}[\mathbf{x}_0|\mathbf{x}_t] - \mathbf{x}_t\|_2$  along sampling trajectories. According to the identity  $\mathbb{E}[\mathbf{x}_0|\mathbf{x}] = \mathbf{x} + \sigma^2 \nabla_{\mathbf{x}} \log p(\mathbf{x}; \sigma)$ , we have  $\|\mathbb{E}[\mathbf{x}_0|\mathbf{x}_t] - \mathbf{x}_t\|_2 = \sigma_t^2 \|\nabla_{\mathbf{x}} \log p(\mathbf{x}_t; \sigma_t)\|_2$ . Our experimental results (Figs. 14) reveal that  $\|\mathbb{E}[\mathbf{x}_0|\mathbf{x}_t] - \mathbf{x}_t\|_2$  scales linearly with  $\sigma_t$  as  $t \rightarrow 0$ , confirming that  $\|\mathbb{E}[\mathbf{x}_0|\mathbf{x}_t] - \mathbf{x}_t\|_2 = O(\sigma_t)$  as  $\sigma_t \rightarrow 0$ .

## A.5. Discussion

While the unique projection assumption (Assumption 1) may appear restrictive, it holds almost surely for sampling trajectories in practice. Theorem 5 establishes that noisy variables  $\mathbf{x}_t$  along sampling trajectories lie outside the manifold  $\Omega$  almost surely, since the forward diffusion process generates a globally supported distribution over  $\mathbb{R}^d$ . These empirical findings corroborate the theoretical prediction that singular score function behavior induces numerical instabilities and approximation errors that accumulate during the early stages of inversion.

Recent work by Pidstrigach (2022) establishes that the projection distance provides a lower bound for  $\|\mathbb{E}[\mathbf{x}_0|\mathbf{x}_t] - \mathbf{x}_t\|$  along sampling trajectories when the data manifold satisfies appropriate geometric regularity conditions. Our validation experiments on canonical low-dimensional distributions—including discrete point clouds and Gaussian distributions on linear subspaces—empirically verify that  $\|\mathbb{E}[\mathbf{x}_0|\mathbf{x}_t] - \mathbf{x}_t\| = O(\sigma_t)$  as  $t \rightarrow 0$ . The normalized quantity  $\|\mathbb{E}[\mathbf{x}_0|\mathbf{x}_t] - \mathbf{x}_t\| / \sigma_t$  converges to a bounded constant, which implies the score function singularity  $\|\nabla_{\mathbf{x}} \log p(\mathbf{x}_t; \sigma_t)\| = O(1/\sigma_t)$  for  $\mathbf{x}_t$  along sampling trajectories, as predicted by Theorem 3. These findings confirm that singular score function behavior in the low-noise regime leads to amplified approximation errors and numerical instabilities during the early stages of inversion, thereby providing theoretical justification for the design choices underlying the SSI inversion algorithm.

## B. Extension to Variance Preserving Processes

While the main text focuses on Variance Exploding (VE) processes for clarity, our Singularity Skipping Inversion (SSI) method extends naturally to Variance Preserving (VP) processes, which are widely used in practice (e.g., DDIM (Song et al., 2021a)). This section presents the mathematical framework for VP processes and demonstrates how SSI applies to this setting with minimal modifications.

### B.1. Mathematical Framework for VP Processes

Following the general framework of Karras et al. (2022), we first define the unscaled forward diffusion process:

$$\mathbf{x}_t = \mathbf{x}_0 + \sigma_t \mathbf{n}, \quad \mathbf{n} \sim \mathcal{N}(\mathbf{0}, \mathbf{I}), \quad (11)$$

where  $\sigma_t = \sigma(t) : [0, T] \rightarrow [0, \infty)$  is a strictly increasing noise schedule with  $\sigma_0 = 0$ . VP processes then introduce a scaling schedule  $s_t = s(t) : [0, T] \rightarrow [0, 1]$  with  $s_t = 1/\sqrt{1 + \sigma_t^2}$  for all  $t$ , where  $s_t$  is strictly decreasing with  $s_0 = 1$ . The scaled variable is defined as  $\tilde{\mathbf{x}}_t = s_t \mathbf{x}_t$ , which gives the forward diffusion process for VP SDEs:

$$\tilde{\mathbf{x}}_t = s_t \mathbf{x}_0 + s_t \sigma_t \mathbf{n}, \quad \mathbf{n} \sim \mathcal{N}(\mathbf{0}, \mathbf{I}), \quad (12)$$

This defines a smoothed distribution family  $p(\tilde{\mathbf{x}}; \sigma)$  that gradually transforms the data distribution to Gaussian noise as  $t$  increases from 0 to  $T$ .

The key difference between VP and VE processes lies in the scaling factor  $s_t$ . For VE processes,  $s_t = 1$  for all  $t$ , so the forward process is simply  $\mathbf{x}_t = \mathbf{x}_0 + \sigma_t \mathbf{n}$  and  $\tilde{\mathbf{x}}_t = \mathbf{x}_t$ . For VP processes, the scaling factor ensures that the variance of the noisy variable remains bounded, hence the name "Variance Preserving."

Following Karras et al. (2022), the probability flow ODE for the scaled variable  $\tilde{\mathbf{x}}$  reads:

$$d\tilde{\mathbf{x}} = \left[ \frac{\dot{s}_t}{s_t} \tilde{\mathbf{x}} - s_t^2 \dot{\sigma}_t \sigma_t \nabla_{\tilde{\mathbf{x}}} \log p \left( \frac{\tilde{\mathbf{x}}}{s_t}; \sigma_t \right) \right] dt, \quad (13)$$

where the score function  $\nabla_{\tilde{\mathbf{x}}} \log p(\tilde{\mathbf{x}}; \sigma)$  guides the denoising process.

### B.2. SSI Method for VP Processes

Our SSI method extends naturally to VP processes with minor modifications. The key insight remains the same: by directly sampling from the noisy distribution at time  $t_{\text{SSI}}$  instead of inverting from  $t = 0$ , we avoid the singular region where score functions blow up.

For VP processes, to invert a real image  $\mathbf{x}_0$ , we first obtain a sample from the noisy distribution at  $t_{\text{SSI}}$ :

$$\tilde{\mathbf{x}}_{t_{\text{SSI}}} = s_{t_{\text{SSI}}} \mathbf{x}_0 + s_{t_{\text{SSI}}} \sigma_{t_{\text{SSI}}} \mathbf{n}, \quad \mathbf{n} \sim \mathcal{N}(\mathbf{0}, \mathbf{I}). \quad (14)$$

This noise injection operation obtains a sample from the noisy distribution  $p(\tilde{\mathbf{x}}; \sigma_{t_{\text{SSI}}})$  at time  $t_{\text{SSI}}$ , which jumps to a corresponding variable on another trajectory. Then, we perform inversion from  $\tau_0 = t_{\text{SSI}}$  to  $\tau_N = T$  using forward Euler discretization. For each step from  $\tau_i$  to  $\tau_{i+1}$ :

$$\tilde{\mathbf{x}}_{\tau_{i+1}} = \tilde{\mathbf{x}}_{\tau_i} + \left[ \frac{\dot{s}_{\tau_i}}{s_{\tau_i}} \tilde{\mathbf{x}}_{\tau_i} - s_{\tau_i}^2 \dot{\sigma}_{\tau_i} \sigma_{\tau_i} \nabla_{\tilde{\mathbf{x}}} \log p \left( \frac{\tilde{\mathbf{x}}_{\tau_i}}{s_{\tau_i}}; \sigma_{\tau_i} \right) \right] \Delta\tau, \quad (15)$$

where the score function is computed using the pre-trained denoising network  $D_\theta$ . The detailed algorithm for VP processes is presented in Algorithm 2.

### B.3. Theoretical Extensions

The theoretical results established for VE processes extend naturally to VP processes. The singularity analysis of score functions (Theorem 3) applies to VP processes as well, since the blow-up behavior is determined by the noise level  $\sigma_t$  rather than the scaling factor  $s_t$ . The key observation is that the score function's singular behavior near  $t = 0$  is characterized by the  $1/\sigma_t$  rate, which is independent of the scaling schedule.

**Algorithm 2** Singularity Skipping Inversion (for VP processes)

**Require:** clean image  $\mathbf{x}_0$ , skipping time  $t_{\text{SSI}}$ , final time  $T$ , time steps  $\{\tau_i\}_{i=0}^N$  with  $\tau_0 = t_{\text{SSI}}$  and  $\tau_N = T$ , pre-trained neural network  $D_\theta$ , scaling schedule  $s_t$ , noise schedule  $\sigma_t$

**Ensure:** A noisy latent  $\tilde{\mathbf{x}}_T$

- 1: Sample  $\mathbf{n} \sim \mathcal{N}(\mathbf{0}, \mathbf{I})$
- 2:  $\tilde{\mathbf{x}}_{t_{\text{SSI}}} \leftarrow s_{t_{\text{SSI}}} \mathbf{x}_0 + s_{t_{\text{SSI}}} \sigma_{t_{\text{SSI}}} \mathbf{n}$
- 3: **for**  $i = 0, 1, \dots, N-1$  **do**
- 4:    $\Delta\tau \leftarrow \tau_{i+1} - \tau_i$
- 5:    $\nabla_{\tilde{\mathbf{x}}} \log p(\tilde{\mathbf{x}}_{\tau_i}/s_{\tau_i}; \sigma_{\tau_i}) \leftarrow (D_\theta(\tilde{\mathbf{x}}_{\tau_i}/s_{\tau_i}, \sigma_{\tau_i}) - \tilde{\mathbf{x}}_{\tau_i}/s_{\tau_i})/\sigma_{\tau_i}^2$
- 6:    $\tilde{\mathbf{x}}_{\tau_{i+1}} \leftarrow \tilde{\mathbf{x}}_{\tau_i} + \left[ \frac{\dot{s}_{\tau_i}}{s_{\tau_i}} \tilde{\mathbf{x}}_{\tau_i} - s_{\tau_i}^2 \dot{\sigma}_{\tau_i} \sigma_{\tau_i} \cdot \nabla_{\tilde{\mathbf{x}}} \log p(\tilde{\mathbf{x}}_{\tau_i}/s_{\tau_i}; \sigma_{\tau_i}) \right] \Delta\tau$
- 7: **end for**
- 8:  $\tilde{\mathbf{x}}_T \leftarrow \tilde{\mathbf{x}}_{\tau_N}$

Similarly, the projection distance concentration result (Theorem 5) extends to VP processes. The geometric properties of the data manifold and the concentration behavior of Gaussian random variables remain unchanged when considering the scaled variable  $\tilde{\mathbf{x}}_t$ .

For the reconstruction error bound (Proposition 4.1), the analysis extends to VP processes with appropriate modifications. The bound scales with  $\sigma_{t_0}$ , confirming that smaller noise injection levels lead to better reconstruction fidelity, just as in the VE case. The tradeoff between reconstruction fidelity and editability also holds for VP processes, with the same qualitative behavior: smaller  $t_0$  improves reconstruction but may compromise editability, while larger  $t_0$  enhances editability at the cost of increased reconstruction error.

**Connection to DDIM** DDIM is a special case of VP processes with a specific discretization scheme. We define  $s_t = \sqrt{\alpha_t}$ ,  $\sigma_t^2 = \frac{1-\alpha_t}{\alpha_t}$  and  $\Delta t = \frac{1}{1000}$ ,  $t_i = i\Delta t$ ,  $i = 1, 2, \dots, 1000$  and using the forward Euler method. We have the following iterative formula:

$$\frac{\tilde{\mathbf{x}}_{t_{i-1}}}{s_{t_{i-1}}} = \frac{\tilde{\mathbf{x}}_{t_i}}{s_{t_i}} + \sigma_{t_i} \nabla_{\mathbf{x}_{t_i}} \log p(\mathbf{x}_{t_i}; \sigma_{t_i}) (\sigma_{t_{i-1}} - \sigma_{t_i}). \quad (16)$$

From Tweedie's formula, we have the following equation:

$$\sigma_{t_i} \nabla_{\mathbf{x}_{t_i}} \log p(\mathbf{x}_{t_i}; \sigma_{t_i}) = \frac{E[\mathbf{x}_{t_0} | \mathbf{x}_{t_i}] - \mathbf{x}_{t_i}}{\sigma_{t_i}}, \quad (17)$$

which also corresponds to the part approximated by the neural network in  $\epsilon_\theta(\tilde{\mathbf{x}}_{t_i}, t_i)$ . Substituting both  $s_t$  and  $\sigma_t$  expressed in terms of  $\alpha$  into the formula, we obtain the following equation:

$$\frac{\tilde{\mathbf{x}}_{t_{i-1}}}{\sqrt{\alpha_{t_{i-1}}}} = \frac{\tilde{\mathbf{x}}_{t_i}}{\sqrt{\alpha_{t_i}}} + \left( \sqrt{\frac{1-\alpha_{t_{i-1}}}{\alpha_{t_{i-1}}}} - \sqrt{\frac{1-\alpha_{t_i}}{\alpha_{t_i}}} \right) \epsilon_\theta(\tilde{\mathbf{x}}_{t_i}, t_i). \quad (18)$$

This corresponds to the iterative process of DDIM. Note that  $\alpha_t$  here is the continuous format of that in DDIM. Set  $\beta_t = 0.1 + 19.9t$ ,  $\beta_i = \beta_{t_i} \Delta t$ ,  $\alpha_i = \prod_{j=1}^i (1 - \beta_j)$ .

Then our SSI method applies directly to DDIM inversion by:

1. Sampling from the noisy distribution at  $t_{\text{SSI}}$  using the DDIM forward process:  $\tilde{\mathbf{x}}_{t_{\text{SSI}}} = \sqrt{\alpha_{t_{\text{SSI}}}} \mathbf{x}_0 + \sqrt{1 - \alpha_{t_{\text{SSI}}}} \mathbf{n}$ , where  $\alpha_t$  is the cumulative product of the noise schedule.
2. Performing inversion from  $t_{\text{SSI}}$  to  $T$  using the DDIM reverse process, avoiding the singular region near  $t = 0$ .

This approach stabilizes DDIM inversion by bypassing the early timesteps where approximation errors accumulate most severely, thereby improving both reconstruction fidelity and the Gaussian properties of the inverted latent. In summary, the SSI method extends naturally from VE processes to general VP processes with minimal modifications. The core algorithmic principle remains unchanged: directly sample from the noisy distribution at  $t_{\text{SSI}}$  to circumvent the singular region, then perform stable inversion from  $t_{\text{SSI}}$  to  $T$ . The theoretical guarantees—including singularity characterization, projection distance concentration, and reconstruction error bounds—all carry over to VP processes, demonstrating the broad applicability of our approach across different diffusion model formulations.

## C. Robustness Analysis

In this section, we present additional experiments to evaluate the robustness of SSI-DM with respect to varying discretization steps and skipping times. We analyze how these parameters influence the reconstruction quality of inverted images using the EDM model.

We conducted our experiments on the EDM model by varying the number of discretization steps and the skipping time  $t_{\text{SSI}}$ . The experiments were performed on 100 randomly sampled images from the validation set (LSUN Bedroom-256), with quantitative results reported in Table 2.

Table 2. Robustness analysis on the impact of discretization steps and skipping time on reconstruction quality. Metrics averaged over 100 images.

Timesteps	$t_{\text{SSI}}$	MSE $\downarrow$	LPIPS $\downarrow$	SSIM $\uparrow$
40	0.0	0.028	0.404	0.626
40	0.01	0.026	0.366	0.693
40	0.1	0.024	0.307	0.741
40	0.2	0.024	0.310	0.731
100	0.0	0.021	0.393	0.621
100	0.01	0.026	0.291	0.760
100	0.1	0.012	0.219	0.824
100	0.2	0.013	0.229	0.805
200	0.0	0.023	0.366	0.640
200	0.01	0.012	0.245	0.797
200	0.1	0.008	0.171	0.862
200	0.2	0.009	0.187	0.840

The results reveal several key insights. First, introducing a non-zero skipping time  $t_{\text{SSI}}$  consistently improves reconstruction quality across all discretization levels compared to the baseline. Second, increasing the number of discretization steps leads to progressive improvements in all metrics. The optimal performance is achieved with 200 timesteps and  $t_{\text{SSI}} = 0.1$ , yielding MSE of 0.008, LPIPS of 0.171, and SSIM of 0.862. These findings demonstrate the robustness of SSI-DM to hyperparameter choices.